Article
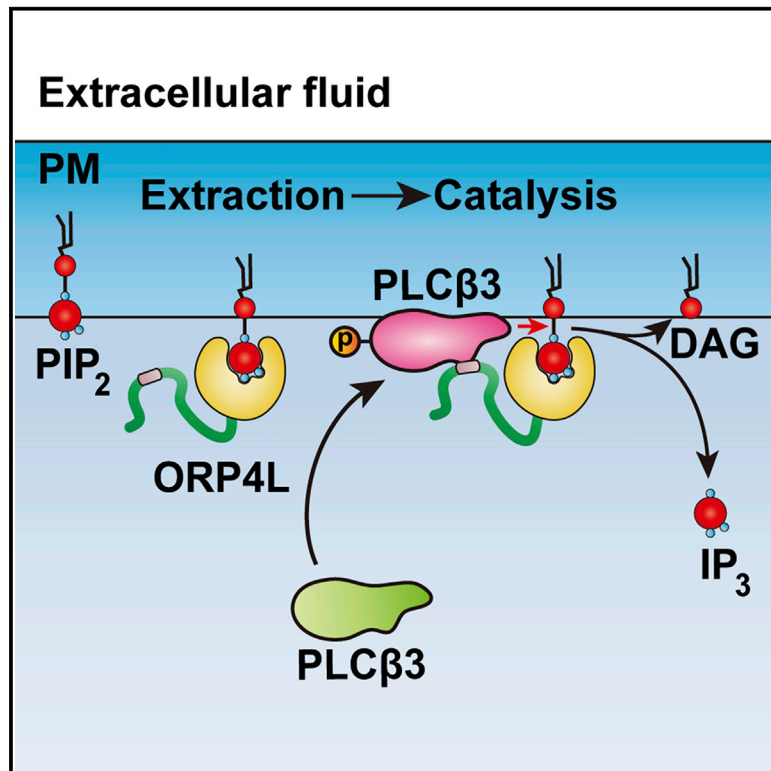
ORP4L Extracts and Presents PIP$_2$ from Plasma Membrane for PLCβ3 Catalysis: Targeting It Eradicates Leukemia Stem Cells

Graphical Abstract

Authors

Wenbin Zhong, Mengyang Xu, Chanjuan Li, ..., Pingsheng Lei, Jun Xu, Daoguang Yan

Correspondence

tydg@jnu.edu.cn

In Brief

Zhong et al. report that abnormal expression of ORP4L is essential for leukemia stem cell survival; it enables IP$_3$ generation by extracting and presenting PIP$_2$ from the plasma membrane to PLCβ3 for hydrolysis. The compound LYZ-81, which blocks this process via targeting ORP4L, selectively eradicates leukemia stem cells.

Highlights

- ORP4L is highly expressed in LSCs and essential for LSC survival

- ORP4L extracts and presents PIP$_2$ from the plasma membrane for PLCβ3 catalysis in LSCs

- LYZ-81 is identified as a specific inhibitor of ORP4L

- Targeting ORP4L by LYZ-81 selectively eradicates LSCs

CellPress

ORP4L Extracts and Presents PIP$_2$ from Plasma Membrane for PLCβ3 Catalysis: Targeting It Eradicates Leukemia Stem Cells

Wenbin Zhong,[1,10] Mengyang Xu,[2,10] Chanjuan Li,[2] Biying Zhu,[1] Xiuye Cao,[1] Dan Li,[1] Huanzhao Chen,[1] Chunxiu Hu,[3] Rong Li,[4] Chengwei Luo,[5] Guoping Pan,[1] Wenqiang Zhang,[1] Chaofeng Lai,[1] Tong Wang,[1] Xin Du,[5] Hong Chen,[6] Guowang Xu,[3] Vesa M. Olkkonen,[7,8] Pingsheng Lei,[9] Jun Xu,[2] and Daoguang Yan[1,11,*]

[1]Key Laboratory of Functional Protein Research of Guangdong Higher Education Institutes, Department of Biology, Jinan University, Guangzhou 510632, China
[2]Research Center for Drug Discovery, School of Pharmaceutical Sciences, Sun Yat-Sen University, Guangzhou 510006, China
[3]CAS Key Laboratory of Separation Science for Analytical Chemistry, Dalian Institute of Chemical Physics, Chinese Academy of Science, Dalian 116011, China
[4]Department of Hematology, Chang Zheng Hospital, Shanghai 200003, China
[5]Department of Hematology, Guangdong General Hospital, Guangdong Academy of Medical Sciences, Guangzhou 510000, China
[6]Boston Children's Hospital, Harvard Medical School, Boston, MA, USA
[7]Minerva Foundation Institute for Medical Research, Biomedicum 2U, Helsinki 00290, Finland
[8]Department of Anatomy, Faculty of Medicine, University of Helsinki, Helsinki 00014, Finland
[9]State Key Laboratory of Bioactive Substances and Functions of Natural Medicines, Chinese Academy of Medical Sciences, Beijing 100050, China
[10]These authors contributed equally
[11]Lead Contact
*Correspondence: tydg@jnu.edu.cn
https://doi.org/10.1016/j.celrep.2019.01.082

SUMMARY

Leukemia stem cells (LSCs) are a rare subpopulation of abnormal hematopoietic stem cells (HSCs) that propagates leukemia and are responsible for the high frequency of relapse in therapies. Detailed insights into LSCs' survival will facilitate the identification of targets for therapeutic approaches. Here, we develop an inhibitor, LYZ-81, which targets ORP4L with high affinity and specificity and selectively eradicates LCSs *in vitro* and *in vivo*. ORP4L is expressed in LSCs but not in normal HSCs and is essential for LSC bioenergetics and survival. It extracts PIP$_2$ from the plasma membrane and presents it to PLCβ3, enabling IP$_3$ generation and subsequent Ca^{2+}-dependent bioenergetics. LYZ-81 binds ORP4L competitively with PIP$_2$ and blocks PIP$_2$ hydrolysis, resulting in defective Ca^{2+} signaling. The results provide evidence that LSCs can be eradicated through the inhibition of ORP4L by LYZ-81, which may serve as a starting point of drug development for the elimination of LSCs to eventually cure leukemia.

INTRODUCTION

Leukemia stem cells (LSCs) are a rare subpopulation of abnormal hematopoietic stem cells that propagates leukemia (Elert, 2013; Lapidot et al., 1994) and is responsible for the high frequency of relapse that is characteristic of current leukemia therapies (Schepers et al., 2015). Initially, LSCs were identified as having the CD34$^+$CD38$^-$ phenotype, similar to normal

hematopoietic stem cells (HSCs) (Bonnet and Dick, 1997). Leukemia initiating and maintaining capacity has been described in other immunophenotypically defined acute myeloid leukemia (AML) subpopulations (Eppert et al., 2011). However, immature CD34$^+$CD38$^-$ cells remain the best-characterized and most potent population initiating leukemia in various xenograft mouse models and retransplantation experiments (Bonnet and Dick, 1997; Eppert et al., 2011; Ishikawa et al., 2007; Lechman et al., 2016; Reya et al., 2001; Saito et al., 2010). LSCs share many properties, such as self-renewal, differentiation potential, and quiescent cell-cycle status, with HSCs (Clevers, 2011; Huntly and Gilliland, 2005). The tendency to remain quiescent renders LSCs resistant to conventional chemotherapeutic agents and radiation, which predominantly target proliferating cells (Huntly and Gilliland, 2005; Tallman et al., 2005). Hence, failure to eradicate quiescent LSCs may result in reinitiating the malignancy after a period of latency. It is therefore crucial to develop therapeutic approaches that target quiescent LSCs.

The second messenger inositol-1,4,5-trisphosphate (IP$_3$) is generated by the hydrolysis of phosphatidylinositol-4,5-bisphosphate (PIP$_2$) located in the plasma membrane (PM) by phospholipase C (PLC) (Rhee et al., 1989). When a ligand binds to a receptor coupled to a Gq heterotrimeric G protein, the α-subunit of Gq induces the activity of PLCβ, resulting in the cleavage of PIP$_2$ into IP$_3$ and diacylglycerol (DAG) (Qin et al., 2011). The binding of IP$_3$ to receptors in the endoplasmic reticulum (ER) results in Ca^{2+} egress and mediates a range of cellular responses (Berridge et al., 2000).

Oxysterol-binding protein (OSBP) and its relatives (ORPs) have emerged as mediators of the interorganelle transfer of cholesterol or phospholipids in exchange for phosphatidylinositol-4-phosphate (PI(4)P) (Mesmin et al., 2013; Tong et al., 2013; Yang, 2006). OSBP mediates sterol and PI(4)P exchange

between the ER and the Golgi (Mesmin et al., 2013), while ORP5/8 exchange phosphatidylserine (PS) for PI(4)P at ER-PM junctions (Chung et al., 2015; Sohn et al., 2018). An essential role of ORP5/8 as a transporter for PIP_2 rather than PI(4)P has recently been explored (Ghai et al., 2017), and ORP2 acts as a selective transporter of cholesterol and PIP_2 at the PM (Wang et al., 2018). Earlier studies suggested that ORP4L may be aberrantly induced in distinct malignant cell types (Charman et al., 2014; Fournier et al., 1999; Henriques Silva et al., 2003). Our recent work showed that ORP4L is expressed in T cell acute lymphoblastic leukemia (T-ALL) cells but not normal T cells and is essential for cell survival (Zhong et al., 2016b). ORP4L controls G protein-coupled IP_3 signaling in T-ALL cells and plays an obligatory role in efficient ATP production via oxidative phosphorylation. However, the mechanism through which ORP4L regulates PLCβ3 catalysis is poorly understood. Given the critical role of ORPs in phosphoinositide metabolism and transport, understanding how ORP4L facilitates IP_3 generation by PLCβ3 is a fundamental and clinically significant question.

In this study, we report that ORP4L executes an essential function in the survival of LSCs: it extracts PIP_2 from the PM and presents it to PLCβ3 for hydrolysis, inaugurating the concept that a PIP_2-presenting cofactor is required for PLC catalysis. Moreover, we explore a compound, LYZ-81, that blocks ORP4L function to eradicate leukemia.

RESULTS

ORP4L Is Selectively Expressed in LSCs, but Not HSCs, and Is Essential for the Survival of LSCs

Our previous study showed that the abnormal expression of ORP4L is essential for T-ALL cell survival (Zhong et al., 2016b). The crucial role of LSCs that propagate leukemia (Lapidot et al., 1994) prompted us to investigate the role of ORP4L in this cell type. LSCs from AML constitute the best-characterized LSC subpopulation (Schepers et al., 2015). We isolated LSCs from the bone marrow of AML patients by using the $CD34^+CD38^-$ markers and validated the stem cell status of the isolated cells (see Method Details). High levels of ORP4L mRNA and protein were detected in all $CD34^+CD38^-$-LSCs specimens, whereas they were absent in HSCs (Figures 1A and 1B).

To investigate a putative role of ORP4L in the LSCs, we carried out knockdown experiments demonstrating that ORP4L depletion reduced the colony-forming capacity of the LSCs (Figure 1C), accelerated the death of LSCs (Figure 1D), and significantly reduced the in vivo engraftment of LSCs in NOD/SCID mice (Figure 1E). To control for possible off-target effects, we carried out a number of RNA interference experiments by using another independent ORP4L small hairpin RNA (shRNA), with similar results (Figures S1A and S1B). The results suggested that ORP4L is expressed in LSCs and is required for the survival of these cells.

LYZ-81 Is a Specific Inhibitor of ORP4L

The role of ORP4L in LSCs survival prompted us to investigate the possibility of targeting ORP4L for leukemia therapy. OSW-1 is an anti-proliferative compound that targets ORP4L and OSBP (Burgett et al., 2011). ORP4L shows a restricted tissue expression pattern, whereas OSBP is ubiquitous (Udagawa et al., 2014). We hypothesized that the toxicity of OSW-1 toward normal cells may be due to its affinity for OSBP; thus, a compound sparing OSBP could be more selective toward cancer cells. To this end, we synthesized OSW-1 analogs, as described (Zheng et al., 2010), and uncovered a compound called LYZ-81 (Figure 2A) that exhibited a drastically more pronounced difference in the half-maximal inhibitory concentration (IC_{50}) toward LSCs versus HSCs (IC_{50} = 3.27 nM in LSCs versus IC_{50} = 1.29 μM in HSCs) than OSW-1 (Figures S2A and S2B). Surface plasmon resonance (SPR) assays demonstrated that LYZ-81 binds ORP4L (K_d = 1.05 ± 0.24 nM; Figure 2B). Homology modeling and molecular docking studies suggested that LYZ-81 binds to ORP4L via hydrogen bonding, forming a stable complex through four residues—Met527, Arg594, Asn600, and Lys681—within the oxysterol-binding domain (ORD) of ORP4L (Figure 2C). To experimentally validate the in silico docking analysis, we constructed an ORP4L mutant, designated ORP4L M4 (Met527Gly, Arg594Gly, Asn600Gly, and Lys681Gly). SPR analyses demonstrated that ORP4L M4 shows a very low affinity for LYZ-81 (Figure S2C), indicating a key role of the four residues in the binding of the compound to ORP4L. This binding mode of LYZ-81 to ORP4L was further supported by experiments in which overexpression of wild-type ORP4L but not ORP4L M4 partly rescued LSCs from death induced by LYZ-81 (Figure 2D). LYZ-81 showed a dose-dependent cytotoxicity toward LSCs at 1–10 nM concentrations, while there was no effect on HSCs even at the highest dose (Figures 2E and 2F; Table S1), as evidenced by the induction of cell death and inhibition serials of colony formation. Together, the data indicate that LYZ-81 eradicates LSCs but not HSCs in vitro.

To address the specificity of LYZ-81 binding to ORP4L, we used SPR assays to determine the binding affinity of OSW-1 and LYZ-81 to ORP4L and OSBP. OSW-1 displays a similar, nanomole binding affinity for these two proteins ($K_{d\ (ORP4L)}$ = 0.85 ± 0.17 nM, $K_{d\ (OSBP)}$ = 1.49 ± 0.26 nM) (Figures S2D and S2E). By contrast, LYZ-81 binds ORP4L with markedly greater affinity than OSBP ($K_{d\ (ORP4L)}$ = 1.05 ± 0.24 nM, $K_{d\ (OSBP)}$ = 5.9 ± 1.86 μM) (Figures 2B and S2F), revealing a strong preference of LYZ-81 for ORP4L. OSW-1 was shown to promote OSBP degradation via a proteasome-dependent pathway (Burgett et al., 2011). To determine whether OSW-1 or LYZ-81 also causes a reduction in the amount of ORP4L, we assessed ORP4L protein levels in compound-treated LSCs by western blotting. Treatment with either compound did not affect ORP4L protein levels (Figure S2G). While OSW-1 induced a dramatic reduction of OSBP in LSCs, no such effect was seen in LYZ-81 treated cells (Figure S2G), adding evidence for the specificity of this compound for ORP4L. Overexpression of either ORP4L or OSBP protected LSCs against cell death induced by OSW-1. However, only ORP4L but not OSBP protected the cells against the cytotoxicity of LYZ-81 (Figure S2H). LYZ-81 executes cytotoxic activity toward LSCs via targeting ORP4L, while sparing OSBP.

To evaluate the cytotoxicity of OSW-1 and LYZ-81 in vivo, OSW-1 (5.8 μg/kg/day, intravenously [i.v.]) or LYZ-81 (5.8 μg/kg/day, i.v.) (Tamura et al., 1997) were injected into mice for
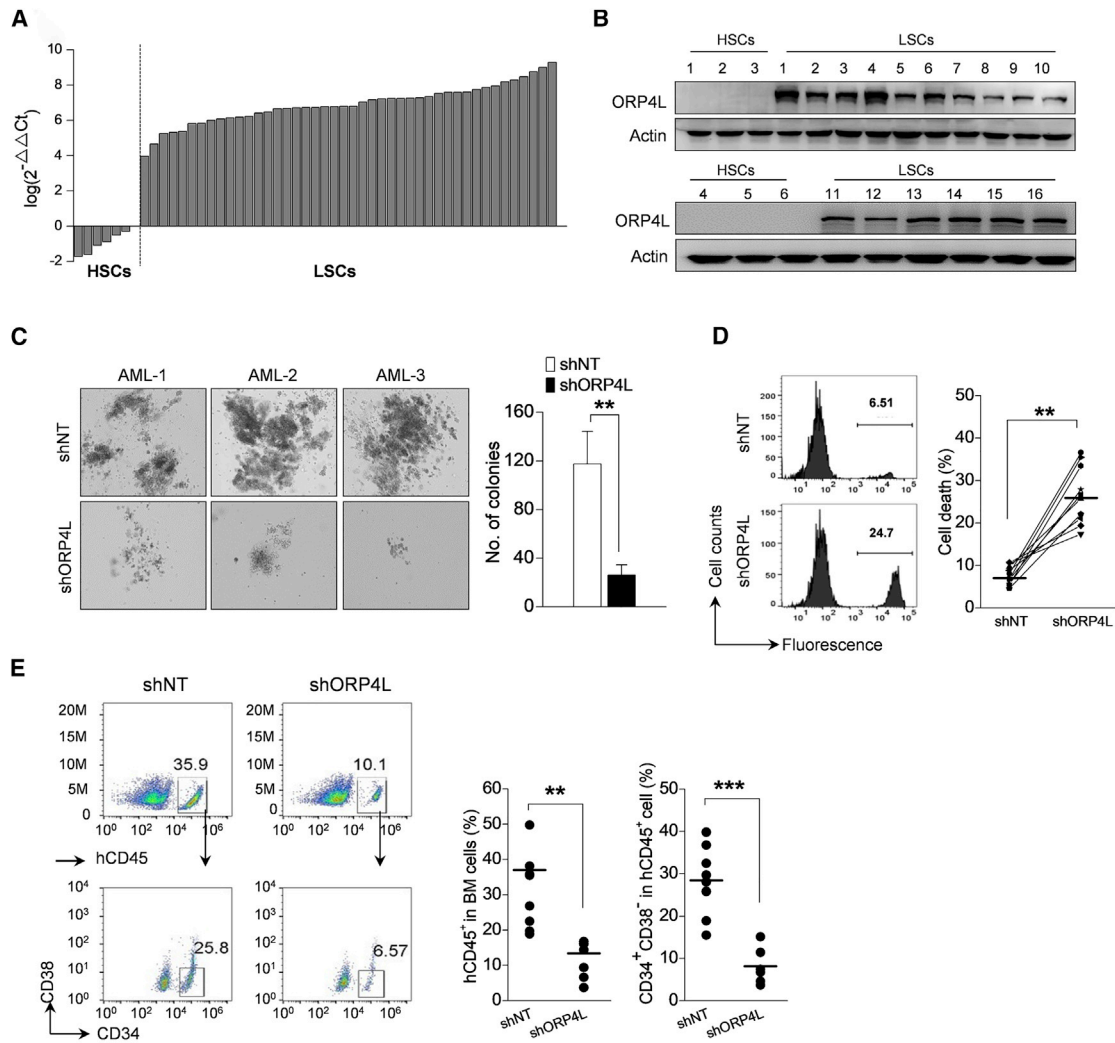
Figure 1. ORP4L Expression in LSCs Is Essential for LSC Survival

(A and B) qPCR (A) and western blot (B) analysis of ORP4L expression in HSCs (n = 6) and LSCs from subjects with AML (n = 45 for qPCR, n = 16 for western blot). Relative gene expression is presented as $\log(2^{-\Delta\Delta Ct})$. The western blot is representative of 3 independent experiments with similar results.

(C) The *in vitro* colony-forming ability of LSCs (n = 3, AML 1, 2, 3 specimens) with ORP4L knockdown. After infection with non-targeting shRNA (shNT) or shORP4L lentivirus for 48 h, the infected cells with GFP were sorted by flow cytometer and plated in Methocult GF and cultured for 14 days. Representative colony microscopy images of the specimens are shown. Mean ± SD values from an experiment performed in triplicate with each specimen are plotted. **p < 0.01, Student's t test.

(D) Cell death analysis in LSCs (n = 10) with ORP4L knockdown. Cells were infected with shNT or shORP4L lentivirus for 120 h before analysis. Representative images of cell death analysis by fluorescence-activated cell sorting (FACS) are shown. The percentage of cell death from independent AML specimens are shown. **p < 0.01, Student's t test.

(E) Percentage of engraftment of leukemia cells (AML 2 specimen) in the bone marrow of NOD/SCID mice (n = 8 for shNT, and n = 6 for shORP4L). Representative images of FACS analysis from one of the mice are shown. The engraftment percentages of leukemia cells from each mouse are plotted. ***p < 0.001, Student's t test.

7 weeks. Histological analysis revealed that LYZ-81 treatment did not alter the gross histology of spleen, bone marrow, heart, brain, kidney, or muscle of the animals (Figure S2I). However, the spleen and bone marrow of OSW-1 treated mice displayed abnormal cell morphology, smaller cell size, and narrowing of intercellular spaces (Figure 2G). These observations are consistent with the view that LYZ-81 is less toxic to normal cells than is OSW-1.

LYZ-81 Preferentially Eradicates LSCs *Ex Vivo* and *In Vivo*

To assess the capacity of LYZ-81 treatment *ex vivo* to reduce LSCs engraftment, we pre-treated AML-CD34+ or umbilical cord (UBC)-CD34+ cells with LYZ-81 and transplanted them into sublethally irradiated NOD/SCID mice (Figure S3A). *Ex vivo* pre-treatment of AML-CD34+ cells with LYZ-81 significantly reduced the engrafted LSCs in mouse bone marrow (Figure S3B).
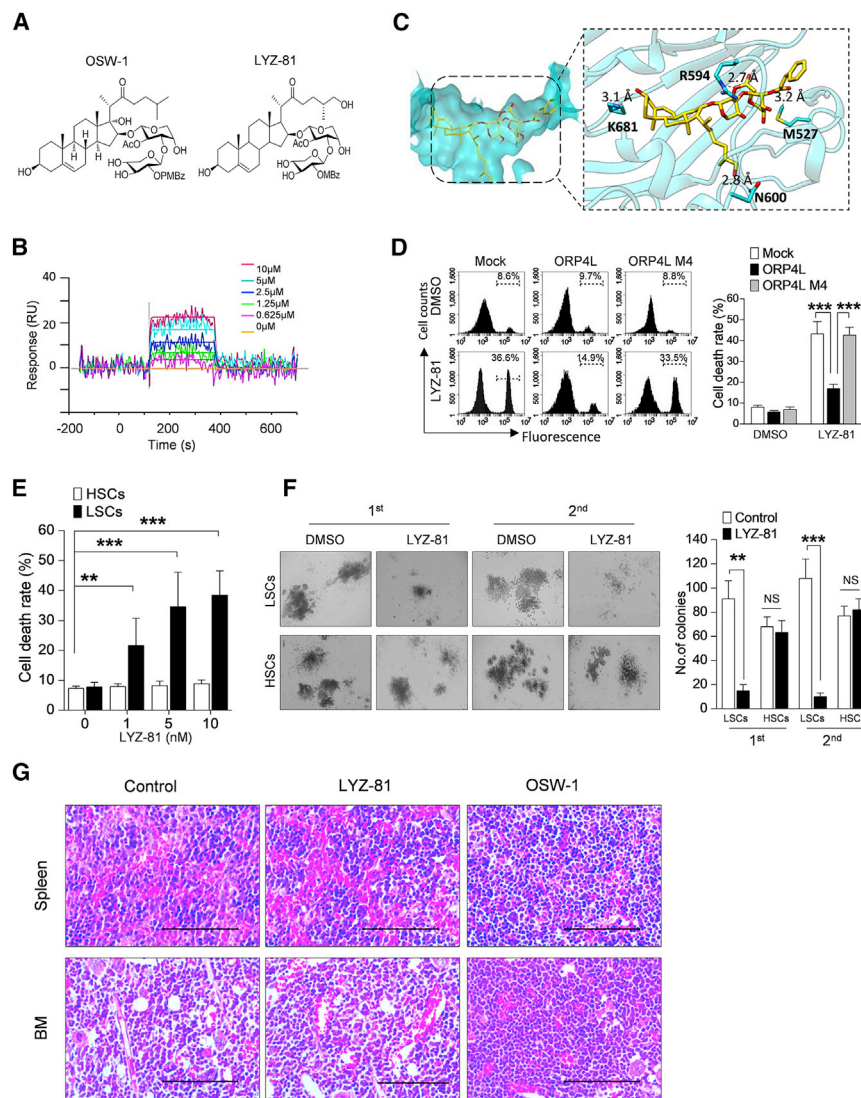
Figure 2. LYZ-81 Selectively Targets ORP4L

(A) The chemical structure of OSW-1 and LYZ-81.

(B) Binding of LYZ-81 to ORP4L in an SPR assay.

(C) Surface representation showing the binding of LYZ-81 to modeled ORP4L.

(D) LSCs (AML 12 specimens) were transfected with empty vector, wild-type ORP4L, or LYZ-81 binding site mutant ORP4L (ORP4L M4) cDNA for 24 h, incubated with or without 5 nM LYZ-81 for 16 h, and evaluated for cell death. Representative images of flow cytometry are shown.

(E) *In vitro* cell death analyses of HSCs (n = 4) and LSCs (n = 13, AML-1, -2, -3, -4, -5, -6, -7, -8, -9, -11, -12, -13, and -14 specimens) treated with increasing concentrations of LYZ-81 are shown. Details of each AML specimen are shown in Table S1.

(F) The *in vitro* colony-forming ability of LSCs in the first and second replanting (n = 5, AML-1, -2, -5, -6, and -10 specimens) and HSCs (n = 4) as examined in the absence or presence of 5 nM LYZ-81. Data are means ± SDs of at least three independent experiments. **p < 0.01, ***p < 0.001, NS, not significant, Student's t test.

(G) H&E stained tissue sections of mice treated with LYZ-81 or OSW-1. The mice were sacrificed after drug treatments at 5.8 μg/kg/day, intraperitoneally (i.p.) for 7 weeks. Similar results were obtained for five mice in each group. Images from one representative mouse per group are shown. Scale bars, 100 μm.

After 7 weeks of therapy, we analyzed the bone marrow of the mice. The LYZ-81 treatment fully eliminated leukemia cells and LSCs from the bone marrow (Figures 3B and 3C). However, LYZ-81 did not reduce the engraftment of HSCs (Figure 3D). Staining of spleen and bone marrow sections with anti-hCD34 supported the notion that LYZ-81 can completely eradicate LSCs *in vivo*

In contrast, engraftment of HSCs was not affected by LYZ-81 treatment (Figure S3C). The decreased engraftment of LYZ-81-treated LSCs was partly rescued by the overexpression of ORP4L before the treatment (Figure S3D), which is consistent with the view that LYZ-81 eliminates LSCs via targeting ORP4L.

To test the therapeutic potential of LYZ-81, we treated NOD/SCID mice engrafted with AML-CD^{34+} or UBC-CD^{34+} cells with LYZ-81 for 7 weeks (Figure 3A). The engrafted leukemia cells and LSCs were determined before and after 1, 2, 4, 5, and 7 weeks of treatment by analyzing peripheral blood leukocytes. Notably, increased numbers of hCD45$^+$ cells and LSCs were found in mice injected with PBS in a series of treatment time courses (Figure S4A), while remarkable reductions in hCD45$^+$ cells and LSCs were evident after 4 and 5 weeks of LYZ-81 treatment. No detectable hCD45$^+$ cells or LSCs were found in the peripheral blood of the animals after LYZ-81 treatment for 7 weeks (Figure S4A). LYZ-81 did not exert a significant reduction in hCD45$^+$ cells or HSCs in mice engrafted with HSCs (Figure S4B).

(Figure 3E). Furthermore, LYZ-81 therapy significantly delayed tumor-related death of the animals (Figure 3F). Thus, pharmacologic inhibition of ORP4L by LYZ-81 markedly and selectively eradicates LSCs both *in vitro* and *in vivo*.

ORP4L Facilitates PIP$_2$ Clearance in the PM

Similar to Jurkat T cells, ORP4L interacts with G$\alpha_{q/11}$ and PLCβ3 upon stromal cell-derived factor 1α (SDF-1α) (a cytokine binding G protein-coupled receptor CXCR4 [Murdoch, 2000]) stimulation in LSCs (Figures S5A and S5B). Knockdown of PLCβ3 significantly reduced IP$_3$ production in LSCs (Figure S5C), indicating that the PLCβ3 isoform plays a dominant role in IP$_3$ production in these cells. ORP4L depletion significantly reduced the spontaneous cytosolic [Ca^{2+}]$_c$ and mitochondrial [Ca^{2+}]$_m$ oscillations (Figure S5D) that are associated with the inactivation of pyruvate dehydrogenase (PDH; Figure S5E), reduction of oxygen consumption rate (OCR), and ATP production (Figure S5F). Furthermore, ORP4L knockdown reduced AMP kinase (AMPK)
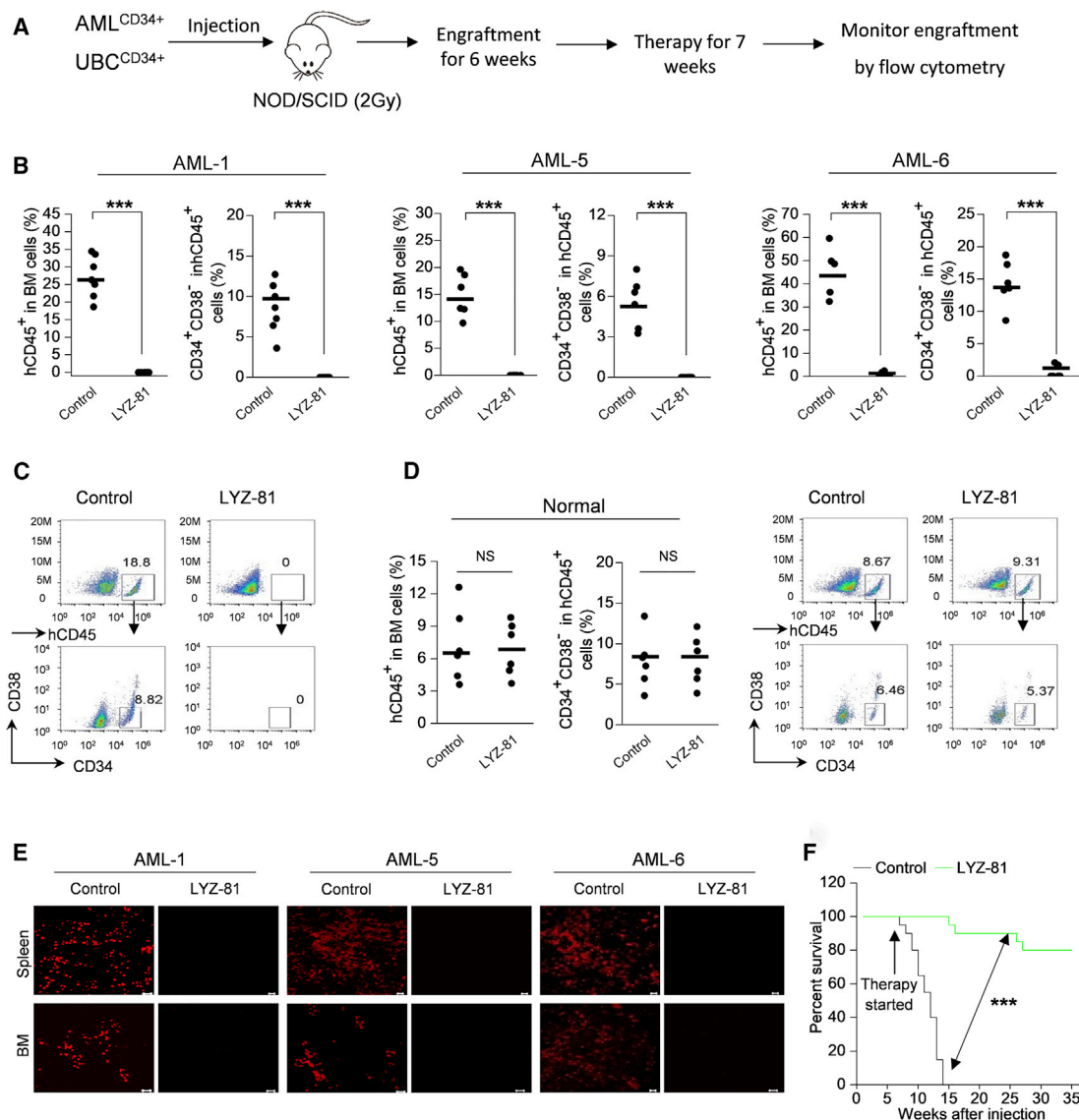
Figure 3. LYZ-81 Eradicates LSCs *In Vivo*

(A) Overview of the experimental design for LYZ-81 therapy after xenotransplantation of LSCs and HSCs into NOD/SCID mice.

(B) Engraftment of human leukemia cells (AML-1, AML-5, and AML-6 specimens) in the bone marrow of NOD/SCID mice after treatment with vehicle control or LYZ-81 (5.8 μg/kg/day, i.v.) for 7 weeks. The percentage engraftment of leukemia cells in each mouse is plotted. ***p < 0.001, Student's t test.

(C) Representative images of flow cytometry from one of the mice are shown.

(D) Engraftment of human normal human cells in the bone marrow of NOD/SCID mice after treatment with vehicle control or LYZ-81 (5.8 μg/kg/day, i.v.) for 7 weeks. The percentage engraftment of HSCs in each mouse is plotted. NS, not significant, Student's t test.

(E) Staining of hCD34 antibody in spleen and bone marrow from mice grafted with untreated or treated AML specimens. Scale bars, 10 μm. Similar results were obtained for the five mice of each group.
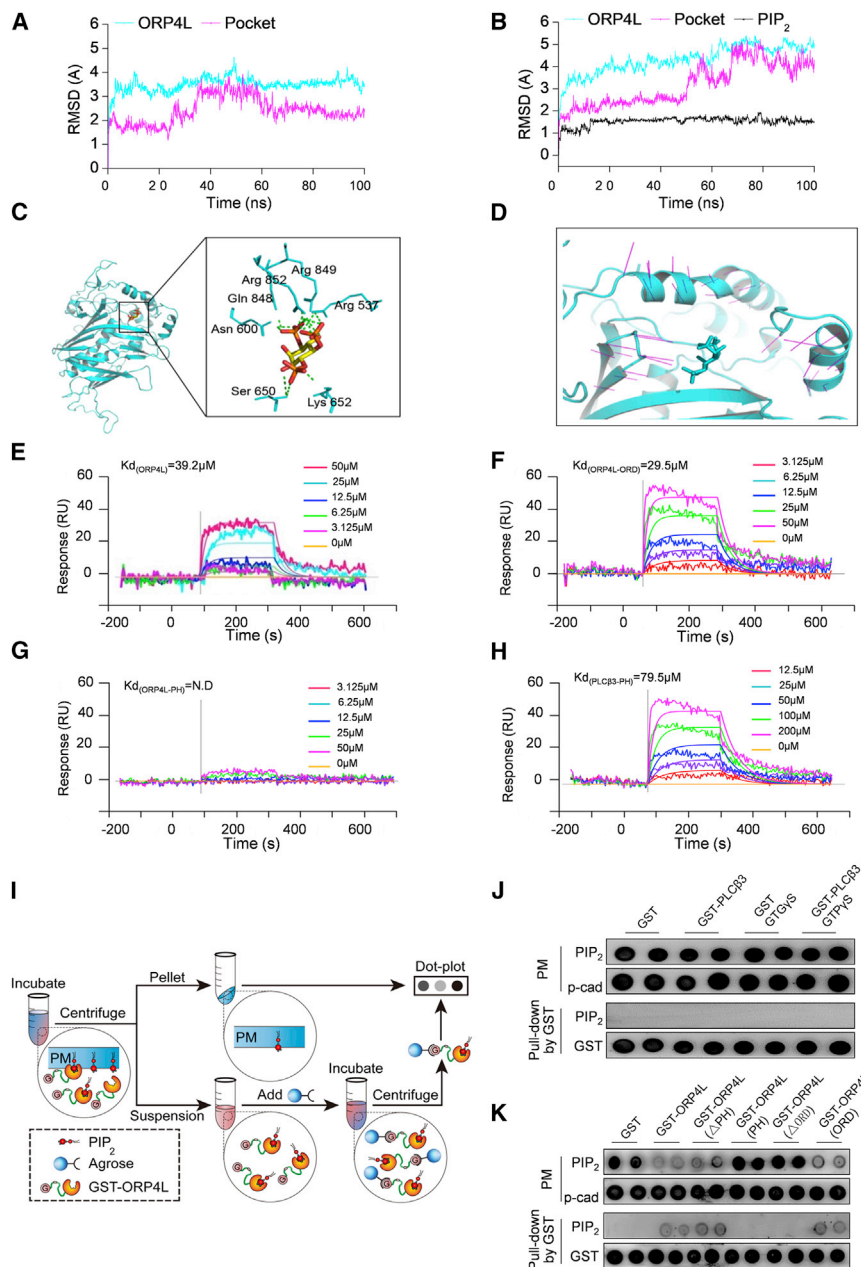
(F) The survival of the mice (n = 10) was compared by Kaplan-Meier analysis, with statistical significance determined by log-rank test. ***p < 0.001.

activation and induced autophagy (Figure S5G). To strengthen the link between ORP4L, Ca^{2+} signaling and mitochondrial metabolism, we used the mitochondrial calcium uniporter (MCU) agonist kaempferol (Montero et al., 2004), which abolished the inactivation of PDH, the elevated autophagy, the reduced OCR, and the dampened ATP production upon ORP4L knockdown (Figure S5H). LSC death was rescued by the inhibitor of autophagy, 3-methyladenine (Figure S5I), indicating that

ORP4L knockdown induced LSC death via an autophagic mechanism.

To identify the function of ORP4L in LSCs, we carried out the following experiments in the CD34+CD38− KG1-α cell line that meets the properties of stem cells (She et al., 2012). ORP4L is highly expressed in CD34+CD38− KG1-α cells (Figure S6A), and its knockdown (Figure S6B) induced cell death (Figure S6C). Prompted by the functions of ORPs as lipid transporters and role

Figure 4. ORP4L Increases PIP$_2$ Clearance at the PM

(A) Heatmap visualization of the significantly changed lipid species in the plasma membrane (PM) of KG1-α cells with ORP4L knockdown. Cells were treated with 500 ng/mL of SDF-1α for 5 min before PM preparation.

(B and C) Kinetics of PM PIP$_2$ decline upon treatment of KG1-α cells (B) or primary LSCs (C, AML-2 specimen) with 500 ng/mL of SDF-1α, upon ORP4L knockdown or overexpression.

(D and E) Representative images of the kinetics of PIP$_2$ clearance in the PM of KG1-α cells with 500 ng/mL of SDF-1α, upon ORP4L knockdown (D) or overexpression (E). Data are means ± SDs of at least 30 cells observed.

of ORP4L with IP$_3$ production at the PM, we isolated PM from control and ORP4L-deficient CD34$^+$CD38$^-$ KG1-α cells. Global lipidomics profiling revealed that phosphatidylinositols (PIs) were significantly enriched, whereas the products of PLC,

DAGs, were reduced upon the loss of ORP4L (Figure 4A), indicating a function of ORP4L in the metabolism of PI at the PM. We therefore measured the kinetics of PIP$_2$ clearance in the PM after ligand stimulation. The PM PIP$_2$ levels declined steadily

Figure 5. ORP4L Extracts PIP₂ from the PM

(A and B) RMSD curves of apo-ORP4L (A) and ORP4L/PIP₂ complex (B).

(C) The binding of PIP₂ to modeled ORP4L by molecular docking.

(D) The binding pocket of ORP4L aligned onto apo-ORP4L. Magenta lines indicate movements from apo-ORP4L to PIP₂-bound ORP4L.

(E–H) Binding of PIP₂ to full-length ORP4L (E), ORP4L-ORD (F), ORP4L-PH (G), and PLCβ3-PH (H) in an SPR assay.

(I) Schematic of the PIP₂ extraction experiments (see Method Details).

(J) Dot-blot to determine the ability of inactivated or activated (with GTPγS) PLCβ3 to extract PIP₂. The PLCβ3 activities are shown in Figure S6E. After reaction, the PIP₂ remaining in the PM were analyzed.

(K) Dot-blot to determine the ability of ORP4L and the indicated truncated ORP4L constructs to extract PIP₂.

square deviation (RMSD) curves, the pocket entrance (residues 520–540, 622–631, and 836–853) of apo-ORP4L expanded during 30–60 ns and then restored a closed conformation (Figure 5A; Video S2). However, as for the ORP4L/PIP₂ complex, the pocket entrance expanded over time (Figure 5B; Video S3). In the privileged conformation, PIP₂ formed hydrogen bonds with specific hydrophilic residues of ORP4L (Arg537, Asn600, Ser650, Lys652, Gln848, Arg849, and Arg852) at the pocket entrance area (Figure 5C). Alignment of ORP4L/PIP₂ with apo-ORP4L revealed that the pocket entrance in ORP4L/PIP₂ expanded (magenta lines in Figure 5D). Immunofluorescence staining showed the co-localization of ORP4L and PIP₂ in KG1-α and LSCs (Figure S6D). SPR assays further confirmed that the full-length ORP4L (Figure 5E) and its ORD (Figure 5F) but not its Pleckstrin homology (PH) domain (Figure 5G) bind PIP₂. The ORD of ORP4L has higher affinity for PIP₂ than the PH domain of PLCβ3 (Figure 5H), indicating a preference of PIP₂ for binding ORP4L.

Given the direct ORP4L/PIP₂ interaction, we postulated that ORP4L may extract PIP₂ from the PM. After incubating PMs with purified glutathione S-transferase (GST)-PLCβ3 or GST-ORP4L proteins, the PMs were collected and the PIP₂ remaining in the membranes was analyzed to monitor the extraction capacity of the proteins (Figure 5I). PLCβ3 was activated by guanosine triphosphate (GTP)γS (Figure S6E), as previously described (Hepler et al., 1993). We found that PLCβ3 (inactive or GTPγS-bound active form) alone was unable to extract PIP₂ (Figure 5J). In contrast, incubation with ORP4L decreased the amount of

after SDF-1α stimulation of KG1-α cells, and ORP4L knockdown reduced (Figures 4B and 4D; Video S1) while ORP4L overexpression accelerated the clearance of PIP₂ (Figures 4B and 4E). Similar effects of ORP4L manipulations on PIP₂ clearance were observed in primary LSCs upon SDF-1α stimulation (Figure 4C).
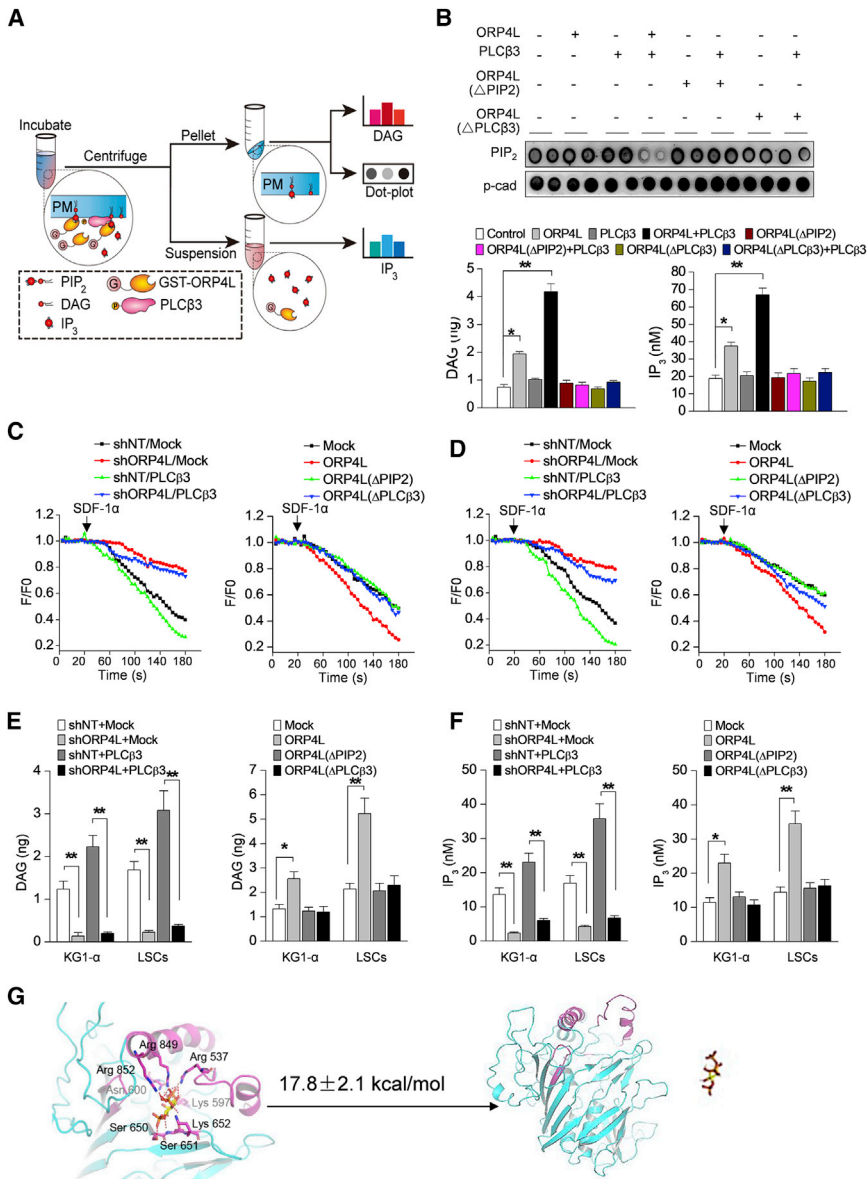
ORP4L Binds and Extracts PIP₂ from the PM

To investigate whether ORP4L regulates PIP₂ clearance at the PM by a direct interaction with PIP₂, the three-dimensional (3D) structure of ORP4L-ORD was predicted through homology modeling and subjected to 100-ns molecular dynamics simulations with the head group of PIP₂. According to root-mean-

Figure 6. ORP4L Presents PIP$_2$ to PLCβ3 for Catalysis

(A) Schematic presentation of the cell-free system experiments (see Method Details).

(B) The amount of PIP$_2$ (top) and DAG in the PM and the IP$_3$ released (bottom) after cell-free reconstituted reactions in the presence of the indicated recombinant proteins.

(C and D) Kinetics of PM PIP$_2$ decline upon treatment of KG1-α cells (C) and primary LSCs (D, AML-2 specimen) with 500 ng/mL of SDF-1α upon the indicated genetic manipulations.

(E and F) DAG (E) in the PM and the IP$_3$ released (F) in KG1-α cells and primary LSCs (AML-2, -6, and -12 specimens) upon the indicated genetic manipulations. Cells were stimulated with 500 ng/mL of SDF-1α for 3 min before analysis.
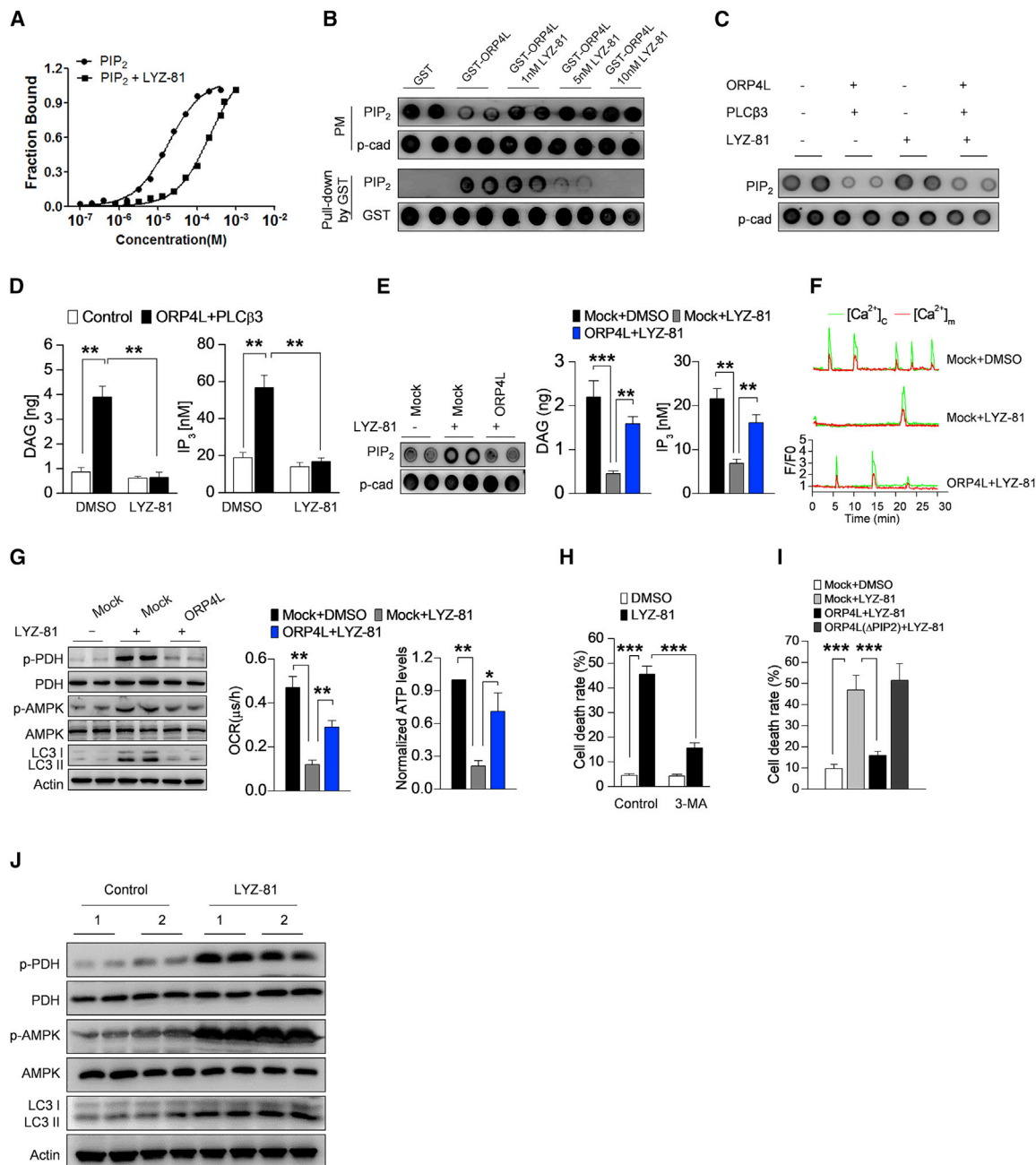
(G) SMD simulations for 2 ns demonstrating the dissociation of IP$_3$ from ORP4L. Data are means ± SDs of at least three independent experiments. *p < 0.05, **p < 0.01, Student's t test.

cally decreased the PIP$_2$ level and concomitantly increased the production of the second messengers. We next generated ORP4L mutants deficient in PIP$_2$ binding (replaced Arg537, Asn600, Ser650, Lys652, Gln848, Arg849, and Arg852 by Gly, ORP4LΔPIP$_2$) and PLCβ3 binding (ORP4LΔPLCβ3) (Zhong et al., 2016a). These two ORP4L mutants abolished the effects of the protein on PIP$_2$, DAG, and IP$_3$ (Figure 6B). In living cells, ORP4L knockdown reduced the clearance of PIP$_2$ (Figures 6C and 6D, left) and decreased the second messengers (Figures 6E and 6F, left) in both KG1-α and LSCs, while PLCβ3 overexpression increased all of these parameters, these effects being abolished upon ORP4L knockdown (Figures 6C and 6D, left; Figures 6E and 6F, left). Our recent work showed that ORP4L is required for PLCβ3 translocation from the nucleus

PIP$_2$ in the PM fraction, with a concomitant increase in its amount bound to the ORP4L (Figure 5K), demonstrating the extraction of PIP$_2$ from the PM by ORP4L. Furthermore, the ORD but not the PH domain of ORP4L was crucial for its PIP$_2$ extraction capacity (Figure 5K).

ORP4L Presents PIP$_2$ to PLCβ3 for Hydrolysis

We next reconstituted a cell-free system to study the hydrolysis of PIP$_2$ in the presence or absence of ORP4L and PLCβ3. To exclude endogenous ORP4L, PMs were isolated from KG1-α cells with 90% knockdown of ORP4L. After the reaction, pellets containing the PM were analyzed for PIP$_2$ and DAG and the supernatants for IP$_3$ (Figure 6A). PLCβ3 alone did not induce the loss of PIP$_2$ or the production of second messengers DAG and IP$_3$. However, the combination of ORP4L and PLCβ3 dramati-

to the PM. In ORP4L knockdown cells, wild-type ORP4L and ORP4LΔPIP$_2$ rescued the PLCβ3 translocation, indicating that abolishing PIP$_2$ binding by ORP4L did not affect the role of ORP4L in PLCβ3 translocation. However, the ORP4LΔPLCβ3 mutant was unable do this (Figure S6F). Overexpression of wild-type ORP4L but not the mutants increased the PIP$_2$ clearance (Figures 6C and 6D, right) and second messenger production (Figures 6E and 6F, right). Although the ORP4LΔPIP$_2$ mutant retained the PLCβ3 translocation ability, the defect of PIP$_2$ hydrolysis in ORP4LΔPIP$_2$ overexpressing cells indicated the requirement of PIP$_2$ extraction and presentation for this catalysis. Of note, IP$_3$ was released after PLC catalysis in our cell-free system and in living cells. To address the dissociation of IP$_3$ from the binding pocket of ORP4L, 2-ns steered molecular dynamics (SMD) were performed on the ORP4L/IP$_3$ complex

Figure 7. LYZ-81 Inhibits PIP$_2$ Hydrolysis by Targeting ORP4L

(A) Microscale thermophoresis analysis of PIP$_2$ binding to ORP4L in the presence or absence of 5 nM LYZ-81.

(B) Dot-blot to determine the ability of ORP4L to extract PIP$_2$ in the presence or absence of a series concentration of LYZ-81.

(C and D) The amount of PIP$_2$ (C) and DAG (D) in the PM and the IP$_3$ produced (D) after cell-free reconstituted reactions in the presence or absence of 5 nM LYZ-81.

(E) The amount of PIP$_2$ (left) and DAG (center) in the PM and the IP$_3$ production (right) in living LSCs (AML-2 specimen) with or without LYZ-81 pre-treatment (5 nM, 4 h). The cells were stimulated for 3 min with SDF-1α (500 ng/mL) before analysis.

(F) Spontaneous [Ca^{2+}]$_c$ and [Ca^{2+}]$_m$ oscillations in control or ORP4L overexpressing LSCs (AML-6 specimen) with or without LYZ-81 pre-treatment (5 nM, 4 h).

(G) Western blot analysis (left) of p-PDH, p-AMPK, and LC3 in control or ORP4L overexpressing LSCs (AML-3 specimen) with or without LYZ-81 treatment (5 nM, 4 h). OCR (center) and ATP (right) levels in control or ORP4L overexpressing LSCs (n = 3, AML-1, -3, and -6 specimens) with or without LYZ-81 treatment (5 nM, 4 h).

(H) Cell death analysis in control and LYZ-81 treated LSCs (5 nM, 16 h, n = 3, AML-1, -3, and -6 specimens) with or without the autophagy inhibitor 3-methyl-adenine (3-MA) (5 mM, 16 h).

(I) Cell death analysis in control and LYZ-81 treated LSCs (5 nM, 16 h, n = 3, AML-1, -3, and -6 specimens) with or without ORP4L or ORP4LΔPIP$_2$ overexpression.

(J) Western blot analysis of p-PDH, p-AMPK, and LC3 in LSCs (AML-6 specimens) isolated from control or LYZ-81 treated mice. Data are means ± SDs of at least three independent experiments. **p < 0.01, ***p < 0.001, Student's t test.

through 100-ns MD simulations. At the beginning, IP$_3$ was bound in the binding pocket of ORP4L at Arg 537, Lys 597, Asn 600, Ser 650, Ser 651, Lys 652, Arg 849, and Arg 852. During the 2-ns SMD simulations, the hydrogen bonds were broken, and IP$_3$ eventually escaped from the binding pocket. Pulling IP$_3$ outside the binding pocket of ORP4L was calculated to cost 17.85 ± 2.10 kcal/mol work (Figure 6G; Video S4).

LYZ-81 Blocks PIP$_2$ Hydrolysis by Targeting ORP4L

We further investigated the detail mechanism of LYZ-81 cytotoxicity. Microscale thermophoresis (MST) indicated that LYZ-81 competed with PIP$_2$ for binding to ORP4L (Figure 7A). In the cell-free reconstituted system, LYZ-81 inhibited the extraction of PIP$_2$ by ORP4L in a dose-dependent manner (Figure 7B) and decreased PM PIP$_2$ clearance and production of the second messengers (Figures 7C and 7D). Similar to ORP4L knockdown, LYZ-81 treatment increased in living LSCs the PM PIP$_2$ levels and reduced second messenger production; these effects were partly rescued by ORP4L overexpression (Figure 7E). Moreover, LYZ-81 treatment decreased the [Ca^{2+}]$_c$ and [Ca^{2+}]$_m$ oscillations (Figure 7F), increased phospho (p)-PDH and p-AMPK, and reduced OCR and ATP production in LSCs (Figure 7G), while ORP4L overexpression consistently reversed these effects. LYZ-81 treatment also induced the autophagic death of the LSCs (Figure 7H). The full-length ORP4L but not ORP4LΔPIP$_2$ rescued the cell death induced by LYZ-81 (Figure 7I), indicating that blocking PIP$_2$ extraction and presentation by ORP4L is the key mechanism underlying LYZ-81 cytotoxicity. Furthermore, we isolated and analyzed the remaining human LSCs from animals grafted with AML-6 (see Figure 3B). LYZ-81 treatment of the engrafted animals reduced the PDH activity and increased the p-AMPK levels and autophagy in these cells (Figure 7J), which is consistent with the view that LYZ-81 eradicates LSCs via an autophagic pathway also in vivo.

DISCUSSION

In this study, we found that ORP4L inhibition selectively eradicated LSCs in vitro and in vivo. ORP4L was found to be expressed selectively in LSCs, but not in normal HSCs, and to play an essential role in the survival of LSCs. The protein is required for PIP$_2$ extraction from the PM and its presentation for PLCβ3 to complete PIP$_2$ hydrolysis, Ca^{2+} release, and subsequent bioenergetics. Through this mechanism, ORP4L was found to maintain the oxidative phosphorylation and survival of LSCs. Meanwhile, we found that this process in LSCs may serve as a target for the development of pharmaceuticals for leukemia therapy.

Reprogramming of energy metabolism has been substantiated as an emerging hallmark and therapeutic target in leukemia (Hainaut and Plymoth, 2013; Hanahan and Weinberg, 2011). However, its targeting in cancer cells is challenging, as the healthy cells depend on the same pathways for energy supply (Hainaut and Plymoth, 2013). ORP4L is expressed in T-ALL cells and LSCs from AML patients but not in T cells or HSCs. We selected AML-LSCs as a target for the investigation of the therapeutic potential of ORP4L. ORP4L knockdown in the LSCs resulted in defective bioenergetics and autophagic death of the

cells; the specific inhibitor of ORP4L, LYZ-81, showed similar effects. LYZ-81 was capable of selectively eradicating engrafted human LSCs from NOD/SCID recipient mice after ex vivo or in vivo treatments. We therefore consider ORP4L to be a potential target of pharmaceuticals for leukemia therapy.

In general, the processes regulating IP$_3$ generation are well mapped and are known to play fundamental roles in a variety of Ca^{2+}-dependent cell signaling pathways. Our study offers the extended insight into PLC catalysis that a cofactor is required for PIP$_2$ extraction from the PM and its presentation for PLC. Our recent study (Zhong et al., 2016b) demonstrated that ORP4L interacts with PLCβ3 in T-ALL cells. Here, ORP4L is found to be expressed selectively in LSCs but not in normal HSCs and to play a critical role in LSCs bioenergetics. It forms a complex with Gα$_{q/11}$ and PLCβ3 to control cytosolic and mitochondrial parallel Ca^{2+} spike oscillations that sustain oxidative phosphorylation. We found that ORP4L extracts PIP$_2$ from the PM, while PLCβ3 is unable to do this. In living KG1-α and LSCs, ORP4L knockdown resulted in the retention of PIP$_2$ in the PM, which could not be reversed by overexpressing PLCβ3. Overexpression of wild-type ORP4L but not mutants deficient in PIP$_2$ or PLCβ3 binding induced PIP$_2$ hydrolysis by PLCβ3. These findings were supported by data from a cell-free reconstituted system. The results indicated that the PIP$_2$ extracted by ORP4L could be delivered to its cognate PLCβ3 via a physical interaction of the two proteins.

Our MD simulations supported the notion that ORP4L accommodates PIP$_2$ within its ORD. In the cell-free system, ORP4L alone could extract PIP$_2$ from the PM, and the addition of PLCβ3 allowed PIP$_2$ hydrolysis, the reaction product DAG remaining in the PM. We thus envision that in living cells, the PLC reaction does not involve complete extraction and accommodation of the PIP$_2$ fatty acyl chains within the ORP4L ORD. We hypothesize that the ORP4L interacts with the membrane-bound PIP$_2$ with the inositol-phosphate-binding cleft at the mouth of the ORD pocket, thereby pulling the PIP$_2$ partly out of the membrane for immediate hydrolysis by the PLCβ3. The DAG produced would thus remain in the PM.

To conclude, our data demonstrate that LYZ-81 selectively eliminates LSCs in vitro and in vivo via the inhibition of ORP4L, suggesting this compound as a starting point of drug development for LSCs elimination in leukemia.

STAR★METHODS

Detailed methods are provided in the online version of this paper and include the following:

- KEY RESOURCES TABLE
- CONTACT FOR REAGENT AND RESOURCE SHARING
- EXPERIMENTAL MODELS AND SUBJECT DETAILS
  - Human specimens and cell line
  - Validation of the stem cell status of the isolated LSCs
  - Animal studies
- METHOD DETAILS
  - Reagents and antibodies
  - Gene transfer
  - Quantitative real-time PCR

- PM preparations
- Lipidomics profiling by UPLC-HRMS
- Protein expression and purification
- Measurement of the kinetics of PIP_2 clearance
- PIP_2 extraction assay
- Reconstituted cell-free system
- Dot blots for PIP_2 levels
- Microscale thermophoresis
- IP_3 and DAG measurement
- Surface plasmon resonance assay
- Molecular docking
- MD simulation
- Binding energy calculation
- Steered MD simulation
- Co-immunoprecipitation
- Immunofluorescence microscopy
- Imaging of parallel $[Ca^{2+}]_c$ and $[Ca^{2+}]_m$ oscillations
- Extracellular flux assays and ATP measurements
- Cell cycle analysis
- Cell death assay
- In vitro colony forming assay
- Hematoxylin and eosin staining
- Western blot analysis
- QUANTIFICATION AND STATISTICAL ANALYSIS

SUPPLEMENTAL INFORMATION

Supplemental Information can be found with this article online at https://doi.org/10.1016/j.celrep.2019.01.082.

AUTHOR CONTRIBUTIONS

D.Y. conceived and designed the experiments. W. Zhong and M.X. performed the experiments with the assistance of T.W., B.Z., X.C., G.P., C. Lai, and W. Zhang. C. Luo, X.D., and R.L. collected and analyzed the clinical data. C. Li and J.X. performed the computer docking experiments. D.L. and Huanzhao Chen purified the proteins. C.H. and G.X. performed the lipidomics. P.L. synthesized LYZ-81 and OSW-1. W. Zhong, V.M.O., and D.Y. analyzed the data and wrote the paper, with assistance from Hong Chen.

DECLARATION OF INTERESTS

The authors declare no competing interests.

REFERENCES

Berridge, M.J., Lipp, P., and Bootman, M.D. (2000). The versatility and universality of calcium signalling. Nat. Rev. Mol. Cell Biol. *1*, 11–21.

Bonnet, D., and Dick, J.E. (1997). Human acute myeloid leukemia is organized as a hierarchy that originates from a primitive hematopoietic cell. Nat. Med. *3*, 730–737.

Burgett, A.W., Poulsen, T.B., Wangkanont, K., Anderson, D.R., Kikuchi, C., Shimada, K., Okubo, S., Fortner, K.C., Mimaki, Y., Kuroda, M., et al. (2011). Natural products reveal cancer cell dependence on oxysterol-binding proteins. Nat. Chem. Biol. *7*, 639–647.

Case, D.A., Darden, T., Cheatham, T., Simmerling, C., Wang, J., Duke, R.E., Luo, R., Walker, R.C., Zhang, W., Merz, K.M., Roberts, B., et al. (2012). AMBER 12, University of California, San Francisco. https://www.researchgate.net/publication/313442058_AMBER_12_University_of_California_San_Francisco.

Charman, M., Colbourne, T.R., Pietrangelo, A., Kreplak, L., and Ridgway, N.D. (2014). Oxysterol-binding protein (OSBP)-related protein 4 (ORP4) is essential for cell proliferation and survival. J. Biol. Chem. *289*, 15705–15717.

Chung, J., Torta, F., Masai, K., Lucast, L., Czapla, H., Tanner, L.B., Narayanaswamy, P., Wenk, M.R., Nakatsu, F., and De Camilli, P. (2015). INTRACELLULAR TRANSPORT. PI4P/phosphatidylserine countertransport at ORP5- and ORP8-mediated ER-plasma membrane contacts. Science *349*, 428–432.

Clark, A.M., and Labute, P. (2007). 2D depiction of protein-ligand complexes. J. Chem. Inf. Model. *47*, 1933–1944.

Clevers, H. (2011). The cancer stem cell: premises, promises and challenges. Nat. Med. *17*, 313–319.

Cornell, W.D., Cieplak, P., Bayly, C.I., Gould, I.R., Merz, K.M., Ferguson, D.M., Spellmeyer, D.C., Fox, T., Caldwell, J.W., and Kollman, P.A. (1995). A Second Generation Force Field for the Simulation of Proteins, Nucleic Acids, and Organic Molecules. J. Am. Chem. Soc. *117*, 5179–5197.

Darden, T., York, D., and Pedersen, L. (1993). Particle mesh Ewald: An N·log(N) method for Ewald sums in large systems. J. Chem. Phys. *98*, 10089.

Elert, E. (2013). Living with leukaemia. Nature *498*, S2–S3.

Eppert, K., Takenaka, K., Lechman, E.R., Waldron, L., Nilsson, B., van Galen, P., Metzeler, K.H., Poeppl, A., Ling, V., Beyene, J., et al. (2011). Stem cell gene expression programs influence clinical outcome in human leukemia. Nat. Med. *17*, 1086–1093.

Fournier, M.V., Guimarães da Costa, F., Paschoal, M.E., Ronco, L.V., Carvalho, M.G., and Pardee, A.B. (1999). Identification of a gene encoding a human oxysterol-binding protein-homologue: a potential general molecular marker for blood dissemination of solid tumors. Cancer Res. *59*, 3748–3753.

Frisch, M.J., Trucks, G.W., Schlegel, H.B., Scuseria, G.E., Robb, M.A., Cheeseman, J.R., Scalmani, G., Barone, V., Mennucci, B., Petersson, G.A., et al. (2009). Gaussian 09, Revision B.01. http://www.rsc.org/suppdata/c5/sc/c5sc02423d/c5sc02423d1.pdf.

Ghai, R., Du, X., Wang, H., Dong, J., Ferguson, C., Brown, A.J., Parton, R.G., Wu, J.W., and Yang, H. (2017). ORP5 and ORP8 bind phosphatidylinositol-4, 5-biphosphate (PtdIns(4,5)P $_2$) and regulate its level at the plasma membrane. Nat. Commun. *8*, 757.

Götz, A.W., Williamson, M.J., Xu, D., Poole, D., Le Grand, S., and Walker, R.C. (2012). Routine Microsecond Molecular Dynamics Simulations with AMBER on GPUs. 1. Generalized Born. J. Chem. Theory Comput. *8*, 1542–1555.

Guzman, M.L., Neering, S.J., Upchurch, D., Grimes, B., Howard, D.S., Rizzieri, D.A., Luger, S.M., and Jordan, C.T. (2001). Nuclear factor-kappaB is constitutively activated in primitive human acute myelogenous leukemia cells. Blood *98*, 2301–2307.

Guzman, M.L., Rossi, R.M., Karnischky, L., Li, X., Peterson, D.R., Howard, D.S., and Jordan, C.T. (2005). The sesquiterpene lactone parthenolide induces apoptosis of human acute myelogenous leukemia stem and progenitor cells. Blood *105*, 4163–4169.

Hainaut, P., and Plymoth, A. (2013). Targeting the hallmarks of cancer: towards a rational approach to next-generation cancer therapy. Curr. Opin. Oncol. *25*, 50–51.

Hanahan, D., and Weinberg, R.A. (2011). Hallmarks of cancer: the next generation. Cell *144*, 646–674.

Henriques Silva, N., Vasconcellos Fournier, M., Pimenta, G., Pulcheri, W.A., Spector, N., and da Costa Carvalho, Mda.G. (2003). HLM/OSBP2 is expressed in chronic myeloid leukemia. Int. J. Mol. Med. *12*, 663–666.

Hepler, J.R., Kozasa, T., Smrcka, A.V., Simon, M.I., Rhee, S.G., Sternweis, P.C., and Gilman, A.G. (1993). Purification from Sf9 cells and characterization of recombinant Gq alpha and G11 alpha. Activation of purified phospholipase C isozymes by G alpha subunits. J. Biol. Chem. *268*, 14367–14375.

Hornak, V., Abel, R., Okur, A., Strockbine, B., Roitberg, A., and Simmerling, C. (2006). Comparison of multiple Amber force fields and development of improved protein backbone parameters. Proteins *65*, 712–725.

Huntly, B.J., and Gilliland, D.G. (2005). Leukaemia stem cells and the evolution of cancer-stem-cell research. Nat. Rev. Cancer *5*, 311–321.

Im, Y.J., Raychaudhuri, S., Prinz, W.A., and Hurley, J.H. (2005). Structural mechanism for sterol sensing and transport by OSBP-related proteins. Nature *437*, 154–158.

Ishikawa, F., Yoshida, S., Saito, Y., Hijikata, A., Kitamura, H., Tanaka, S., Nakamura, R., Tanaka, T., Tomiyama, H., Saito, N., et al. (2007). Chemotherapy-resistant human AML stem cells home to and engraft within the bone-marrow endosteal region. Nat. Biotechnol. *25*, 1315–1321.

Lapidot, T., Sirard, C., Vormoor, J., Murdoch, B., Hoang, T., Caceres-Cortes, J., Minden, M., Paterson, B., Caligiuri, M.A., and Dick, J.E. (1994). A cell initiating human acute myeloid leukaemia after transplantation into SCID mice. Nature *367*, 645–648.

Lechman, E.R., Gentner, B., Ng, S.W.K., Schoof, E.M., van Galen, P., Kennedy, J.A., Nucera, S., Ciceri, F., Kaufmann, K.B., Takayama, N., et al. (2016). miR-126 Regulates Distinct Self-Renewal Outcomes in Normal and Malignant Hematopoietic Stem Cells. Cancer Cell *29*, 602–606.

Li, J., Tanhehco, E.J., and Russell, B. (2014). Actin dynamics is rapidly regulated by the PTEN and PIP2 signaling pathways leading to myocyte hypertrophy. Am. J. Physiol. Heart Circ. Physiol. *307*, H1618–H1625.

Lomasney, J.W., Cheng, H.F., Wang, L.P., Kuan, Y., Liu, S., Fesik, S.W., and King, K. (1996). Phosphatidylinositol 4,5-bisphosphate binding to the pleckstrin homology domain of phospholipase C-delta1 enhances enzyme activity. J. Biol. Chem. *271*, 25316–25326.

McCall, M.N., McMurray, H.R., Land, H., and Almudevar, A. (2014). On nondetects in qPCR data. Bioinformatics *30*, 2310–2316.

Mesmin, B., Bigay, J., Moser von Filseck, J., Lacas-Gervais, S., Drin, G., and Antonny, B. (2013). A four-step cycle driven by PI(4)P hydrolysis directs sterol/PI(4)P exchange by the ER-Golgi tether OSBP. Cell *155*, 830–843.

Miyamoto, S., and Kollman, P.A. (1992). Settle: An analytical version of the SHAKE and RATTLE algorithm for rigid water models. J. Comput. Chem. *13*, 952–962.

Montero, M., Lobatón, C.D., Hernández-Sanmiguel, E., Santodomingo, J., Vay, L., Moreno, A., and Alvarez, J. (2004). Direct activation of the mitochondrial calcium uniporter by natural plant flavonoids. Biochem. J. *384*, 19–24.

Mukherjee, G., Patra, N., Barua, P., and Jayaram, B. (2011). A fast empirical GAFF compatible partial atomic charge assignment scheme for modeling interactions of small molecules with biomolecular targets. J. Comput. Chem. *32*, 893–907.

Murdoch, C. (2000). CXCR4: chemokine receptor extraordinaire. Immunol. Rev. *177*, 175–184.

Qin, K., Dong, C., Wu, G., and Lambert, N.A. (2011). Inactive-state preassembly of G(q)-coupled receptors and G(q) heterotrimers. Nat. Chem. Biol. *7*, 740–747.

Reya, T., Morrison, S.J., Clarke, M.F., and Weissman, I.L. (2001). Stem cells, cancer, and cancer stem cells. Nature *414*, 105–111.

Rhee, S.G., Suh, P.G., Ryu, S.H., and Lee, S.Y. (1989). Studies of inositol phospholipid-specific phospholipase C. Science *244*, 546–550.

Ryckaert, J.-P., Ciccotti, G., and Berendsen, H.J.C. (1977). Numerical integration of the cartesian equations of motion of a system with constraints: molecular dynamics of n-alkanes. J. Comput. Phys. *23*, 327–341.

Saito, Y., Kitamura, H., Hijikata, A., Tomizawa-Murasawa, M., Tanaka, S., Takagi, S., Uchida, N., Suzuki, N., Sone, A., Najima, Y., et al. (2010). Identification of therapeutic targets for quiescent, chemotherapy-resistant human leukemia stem cells. Sci. Transl. Med. *2*, 17ra9.

Salomon-Ferrer, R., Götz, A.W., Poole, D., Le Grand, S., and Walker, R.C. (2013). Routine Microsecond Molecular Dynamics Simulations with AMBER on GPUs. 2. Explicit Solvent Particle Mesh Ewald. J. Chem. Theory Comput. *9*, 3878–3888.

Schepers, K., Campbell, T.B., and Passegué, E. (2015). Normal and leukemic stem cell niches: insights and therapeutic opportunities. Cell Stem Cell *16*, 254–267.

She, M., Niu, X., Chen, X., Li, J., Zhou, M., He, Y., Le, Y., and Guo, K. (2012). Resistance of leukemic stem-like cells in AML cell line KG1a to natural killer cell-mediated cytotoxicity. Cancer Lett. *318*, 173–179.

Sohn, M., Korzeniowski, M., Zewe, J.P., Wills, R.C., Hammond, G.R.V., Humpolickova, J., Vrzal, L., Chalupska, D., Veverka, V., Fairn, G.D., et al. (2018). PI(4,5)P$_2$ controls plasma membrane PI4P and PS levels via ORP5/8 recruitment to ER-PM contact sites. J. Cell Biol. *217*, 1797–1813.

Tallman, M.S., Gilliland, D.G., and Rowe, J.M. (2005). Drug therapy for acute myeloid leukemia. Blood *106*, 1154–1163.

Tamura, K., Honda, H., Mimaki, Y., Sashida, Y., and Kogo, H. (1997). Inhibitory effect of a new steroidal saponin, OSW-1, on ovarian functions in rats. Br. J. Pharmacol. *121*, 1796–1802.

Tong, J., Yang, H., Yang, H., Eom, S.H., and Im, Y.J. (2013). Structure of Osh3 reveals a conserved mode of phosphoinositide binding in oxysterol-binding proteins. Structure *21*, 1203–1213.

Udagawa, O., Ito, C., Ogonuki, N., Sato, H., Lee, S., Tripvanuntakul, P., Ichi, I., Uchida, Y., Nishimura, T., Murakami, M., et al. (2014). Oligo-astheno-teratozoospermia in mice lacking ORP4, a sterol-binding protein in the OSBP-related protein family. Genes Cells *19*, 13–27.

Wang, J., Wang, W., Kollman, P.A., and Case, D.A. (2006). Automatic atom type and bond type perception in molecular mechanical calculations. J. Mol. Graph. Model. *25*, 247–260.

Wang, H., Ma, Q., Qi, Y., Dong, J., Du, X., Rae, J., Wang, J., Wu, W.F., Brown, A.J., Parton, R.G., et al. (2018). ORP2 Delivers Cholesterol to the Plasma Membrane in Exchange for Phosphatidylinositol 4, 5-Bisphosphate (PI(4,5)P2). Mol Cell. Published online December 10, 2018. https://doi.org/10.1016/j.molcel.2018.11.014.

Yang, H. (2006). Nonvesicular sterol transport: two protein families and a sterol sensor? Trends Cell Biol. *16*, 427–432.

Zheng, D., Zhou, L., Guan, Y., Chen, X., Zhou, W., Chen, X., and Lei, P. (2010). Synthesis of cholestane glycosides bearing OSW-1 disaccharide or its 1–>4-linked analogue and their antitumor activities. Bioorg. Med. Chem. Lett. *20*, 5439–5442.

Zhong, W., Pan, G., Wang, L., Li, S., Ou, J., Xu, M., Li, J., Zhu, B., Cao, X., Ma, H., et al. (2016a). ORP4L Facilitates Macrophage Survival via G-Protein-Coupled Signaling: ORP4L-/- Mice Display a Reduction of Atherosclerosis. Circ. Res. *119*, 1296–1312.

Zhong, W., Yi, Q., Xu, B., Li, S., Wang, T., Liu, F., Zhu, B., Hoffmann, P.R., Ji, G., Lei, P., et al. (2016b). ORP4L is essential for T-cell acute lymphoblastic leukemia cell survival. Nat. Commun. *7*, 12702.

STAR★METHODS

KEY RESOURCES TABLE

REAGENT or RESOURCE	SOURCE	IDENTIFIER
Antibodies		
Rabbit polyclonal anti-ORP4L	Sigma-Aldrich	Cat#HPA021514; RRID:AB_1854813
Rabbit polyclonal anti-Pyruvate Dehydrogenase E1-alpha subunit [p Ser293]	Novus	Cat# NB110-93479; RRID:AB_1237282
Rabbit polyclonal anti-Pyruvate Dehydrogenase	Cell Signaling	Cat#2784; RRID:AB_2162928
Rabbit monoclonal anti-AMPK-alpha, phospho (Thr172) Clone 40H9	Cell Signaling	Cat#2535; RRID:AB_331250
Rabbit polyclonal anti-LC3B	Cell Signaling	Cat#2775; RRID:AB_915950
Rabbit polyclonal anti-AMPK (23A3)	Cell Signaling	Cat# 2603; RRID:AB_10841287
Mouse monoclonal anti-ACTB	Proteintech Group	Cat# 60008-1-Ig; RRID:AB_2289225
Purified Anti-PtdIns (4,5)P_2 IgM	Echelon Biosciences	Cat# Z-P045; RRID:AB_427225
Goat anti-pan-cadherin (C-19)	Santa Cruz	Cat# sc-1499; RRID:AB_630957
Mouse monoclonal anti-human Ki-67 antibody	BioLegend	Cat# 350526; RRID:AB_2562872
Alexa Fluor 647 mouse monoclonal anti-human CD45 Antibody	BioLegend	Cat# 304026; RRID:AB_893337
Secondary Antibody (Goat Anti-Rabbit Antibody Conjugated to Horseradish Peroxidase)	Bio-Rad /AbD Serotec	Cat# 166-2408EDU; RRID:AB_11125345
Secondary Antibody (Goat Anti-Mouse IgG (H+L)-HRP Conjugate antibody)	Bio-Rad /AbD Serotec	Cat# 170-6516; RRID:AB_11125547
Secondary Antibody (Rabbit Anti-Goat IgG (H+L)-HRP Conjugate antibody)	Bio-Rad /AbD Serotec	Cat# 172-1034; RRID:AB_11125144
Goat polyclonal anti-Rabbit IgG (H+L) Cross-Adsorbed Secondary Antibody, Alexa Fluor 546	Thermo Fisher Scientific	Cat# A-11035; RRID:AB_143051
Donkey polyclonal anti-Goat IgG (H+L) Cross-Adsorbed Secondary Antibody, Alexa Fluor 647	Thermo Fisher Scientific	Cat# A-21469; RRID:AB_2535872
Goat polyclonal anti-mouse IgG (H+L) Cross-Adsorbed Secondary Antibody, Alexa Fluor 488	Thermo Fisher Scientific	Cat#A-11001; RRID:AB_2534069
Mouse monoclonal anti-Human CD38 Antibody, FITC Conjugated	Miltenyi Biotec	Cat# 130-092-259; RRID:AB_615091
Mouse monoclonal anti-Human CD34 Antibody, PE Conjugated	Miltenyi Biotec	Cat# 130-081-002; RRID:AB_244351
Bacterial and Virus Strains		
E. coli DH5α	Vazyme Biotech	Cat#C502-02/03
E. coli BL21 (DE3)	Vazyme Biotech	Cat#C504-02/03
Lentivirus	Shanghai GenePharma	http://www.genepharma.com/En/
Biological Samples		
Human AML bone marrow samples	Department of Hematology, Guangdong General Hospital, Guangdong Academy of Medical Sciences	http://www.gdghospital.org.cn/EN/Index.php
Human normal bone marrow samples	Department of Hematology, Chang Zheng Hospital, Shanghai	http://www.shcz.com/front/officeShow.aspx?id=6
Normal umbilical cord (UCB) blood	Department of Hematology, Guangdong General Hospital, Guangdong Academy of Medical Sciences	http://www.gdghospital.org.cn/EN/Index.php

(*Continued on next page*)

Continued

REAGENT or RESOURCE	SOURCE	IDENTIFIER
Chemicals, Peptides, and Recombinant Proteins		
TRIzol Regent	Thermo Fisher Scientific	Cat#15596026
RNase inhibitor	TaKaRa	Cat#2313A
Penicillin-Streptmycin Solution	HyClone	Cat# SV30010
Fetal bovine serum	Collected In Australia	Cat#JRFBS-04
Iscove's Modified Dulbecco's Medium (IMDM)	GIBCO (life)	Cat#12440-053
Methocult GF H4534	STEMCELL Technologies	Cat#04534
Stem Span SFEM	STEMCELL Technologies	Cat#09600
Cryostor CS10	BioLife Solutions	Cat#210373
rIL3	PeproTech	Cat#AF-200-03
rFlt3	PeproTech	Cat#300-19
rSCF	PeproTech	Cat#300-07
Protease Inhibitor Cocktail	Roche Group	REF 11697498001
SDF-1 α	R&D systems	Cat#350-NS-050
Fluo-4 AM	Thermo Fisher Scientific	Cat#F14217
Rhod-2 AM	Thermo Fisher Scientific	Cat#R1244
3-MA	Selleck	Cat#S2767
Kaempferol	Selleck	Cat#S2314
Compound C	EMD Chemicals	Cat#171260-10MG
7-AAD	Thermo Fisher Scientific	Cat#A1310
OCT embedding medium	Sakura	Cat#4583
OSW-1	This paper	N/A
LYZ-81	This paper	N/A
Recombinant ORP4L protein	This paper	N/A
Recombinant OSBP protein	This paper	N/A
Recombinant PLCβ3protein	This paper	N/A
Critical Commercial Assays		
EasyScript First-Strand cDNA Synthesis SuperMix	TransGen Biotech	Cat# AE301-03
GoTaq qPCR Master Mix	Promega	Cat# A6002
Oxygen Consumption Rate Assay Kit	Cayman Chemical	Cat#600800
ATP Bioluminescence Assay Kit CLS II	Roche	Cat#11699695001
LIVE/DEAD Fixable Far Red Dead Cell Stain Kit	Thermo Fisher Scientific	Cat#L10120
HitHunter Inositol(1,4,5)-Trisphosphate Assay Kit	DiscoverRx Tech	Cat#90-0037
BD Fixation/Permeabilization kit	BD Biosciences	Cat#554714
Isolation of CD34$^+$CD38$^-$ cells Kit	Miltenyi Biotec	Cat#130-056-701
Anti-FITC MicroBeads	Miltenyi Biotec	Cat#130-048-701
Nucleofector Kits for Human CD34$^+$ cells	Lonza	Cat#VPA-1003
Bio-Rad (Hercules, CA) Dc Assay	Bio-Rad	Cat#500-0119
Experimental Models: Cell Lines		
KG1-α cells	ATCC	TIB-152
Experimental Models: Organisms/Strains		
NOD/SCID mouse strain	Nanjing Biomedical Research Institute, China	http://www.nbri-nju.com/
Oligonucleotides		
The shRNA sequences used	Table S3	N/A
Oligonucleotide primers used	Table S3	N/A
Recombinant DNA		
Recombinant cDNA constructs	Table S3	N/A

(*Continued on next page*)

Continued

REAGENT or RESOURCE	SOURCE	IDENTIFIER
Software and Algorithms		
FlowJo_V10 software	FlowJo	https://www.flowjo.com
ImageJ	NIH public software	https://imagej.nih.gov/ij/
Molecular Operating Environment (MOE), 2013.08	Chemical Computing Group	http://www.chemcomp.com

CONTACT FOR REAGENT AND RESOURCE SHARING

Further information and requests for resources and reagents should be directed to and will be fulfilled by the Lead Contact, Daoguang Yan (tydg@jnu.edu.cn).

EXPERIMENTAL MODELS AND SUBJECT DETAILS

Human specimens and cell line

This study was approved by the institutional ethics committee of Jinan University and was performed in accordance with the Declaration of Helsinki. Normal umbilical cord (UCB) blood and human AML bone marrow samples were obtained after obtaining written informed consent at Guangdong General Hospital, Guangzhou and Department of Hematology, Chang Zheng Hospital, ShangHai. The clinical information and the applications for which each sample was used are provided in Table S2. The AML and normal UCB cells were isolated and processed as previously described (Guzman et al., 2001). The samples were collected and subjected to Ficoll-Paque density gradient separation to isolate mononuclear cells, followed by $CD34^+CD38^-$ cells isolation by using MACS enrichment kit (Milltenyi Biotec, Auburn, CA) according to the manufacturer's manual, within 12 h of collection. The purity of the enriched $CD34^+CD38^-$ cells was monitored by staining the cells with FITC conjugated anti-Human CD38 antibody (1:100; Miltenyi Biotec Cat# 130-092-259) and PE conjugated anti-Human CD34 antibody (1:100; Miltenyi Biotec Cat# 130-081-002), and analyzed by flow cytometry. The samples were cryopreserved in freezing medium consisting of Cryostor CS10 (BioLife Solutions, Bothell, WA). Upon thawing, the cells were cultured in Serum-Free Medium (STEMCELL Technologies, Vancouver, BC, Canada) supplemented with 10 ng/mL rIL3 (PeproTech, Rocky Hill, NJ), 10 ng/mL rFlt3 (PeproTech, Rocky Hill, NJ), and 25 ng/mL rSCF (PeproTech, Rocky Hill, NJ) at 37°C in a humidified atmosphere containing 5% CO_2. Leukemic stem-like $CD34^+CD38^-$ KG1-α cells were isolated from KG1-α cells purchased from American Type Culture Collection by using MACS enrichment kit. This cell line was authenticated by Promega short-tandem repeat analysis and tested for mycoplasma contamination before experiments. Cells were cultured in IMDM supplemented with 10% FBS and 100 units/mL penicillin and 100 mg/mL streptomycin in a humidified atmosphere containing 5% CO_2.

Validation of the stem cell status of the isolated LSCs

To characterize ORP4L in LSCs, we enriched $CD34^+CD38^-$ LSCs with purity greater than 95% from AML patients, predominantly representing quiescent G_0 cells (Figure S7A). *In vitro* colony-forming unit (CFU) assays indicated that the isolated LSCs are able to produce colonies after at least four re-plating (Figure S7B). Serial transplantation of LSCs from three individual AML specimens (i.e., successful engraftment in bone marrow of NOD/SCID mice) was readily evident after the 1st transplantation (Figures S7C and S7D). Injection of LSCs purified from the 1st engrafted mice resulted in successful engraftment in the 2nd recipients. The transplanted LSCs gave rise to $CD34^+CD38^-$, $CD34^-$ and $CD34^+CD38^+$ non-stem AML cells in the 1st and 2nd recipients, indicating the long-term engraftment and differentiation capacity of our purified LSCs. Moreover, immunofluorescence staining of bone marrow and spleen sections with anti-hCD34 showed infiltration of human AML cells in the transplant recipient mice (Figure S7E).

Animal studies

NOD/SCID mice were obtained from Nanjing Biomedical Research Institute of Nanjing University and kept under pathogen-free conditions in the Laboratory Animal Center, Jinan University. All procedures were performed based on the UCLA Animal Research Committee-approved protocols. 4 week-old female mice were sublethally irradiated with 11 rad/g by a ^{137}Cs irradiator (Gammacell 3000 Elan, Best Theratronics, Kanata, ON, Canada) and used for transplantation within 24 h.

For experiments in Figure 1E, AML-$CD34^+$ cells were infected with shNT and shORP4L lentivirus for 48 h, the infected cells with GFP were sorted by flow cytometry; for experiments in Figure S3A, AML-$CD34^+$ and UCB-$CD34^+$ cells pre-incubated with 5 nM LYZ-81 for 4 h. NOD/SCID mice were injected with 1×10^7 treated cells via the tail vein in a final volume of 0.2 mL of PBS with 0.5% FBS. Engraftment was assessed 8 weeks after transplantation by Alexa Fluor® 647 conjugated anti-human CD45 antibody (1:100; BioLegend Cat# 304026), FITC conjugated anti-Human CD38 antibody (1:100; Miltenyi Biotec Cat# 130-092-259) and PE conjugated anti-Human CD34 antibody (1:100; Miltenyi Biotec Cat# 130-081-002) staining of bone marrow cells.

For *in vivo* therapy in Figures 3A and 1 × 10^7 AML-CD34$^+$ cells were injected into irradiated NOD/SCID mice via the tail vein in a final volume of 0.2 mL of PBS with 0.5% FBS. After 6 weeks, the successful engraftment of human cells in peripheral blood was detected by flow cytometry, and then these mice were randomly assigned into 2 groups, and treated for 7 weeks with PBS or LYZ-81 (5.8 μg/kg/d, i.v.) (Tamura et al., 1997) each day. Disease evolution and effect of drugs on the HSC-enriched and LSC-enriched compartments were determined after 7 weeks of treatment by flow cytometric analysis of human CD45$^+$CD34$^+$CD38$^-$ cells in bone marrow. All of the animal experiments were repeated at least once.

For primary and serial xenogeneic transplantation of Figure S7C, 2 × 10^6 AML-CD34$^+$CD38$^-$ cells from patients were injected into NOD/SCID mice via the tail vein in a final volume of 0.2 mL of PBS with 0.5% FBS. 6 weeks after transplantation, primary recipient mice were sacrificed, the engraftments were analyzed by staining of bone marrow cells. The bone marrow of primary recipient mice were also collected, purified by using human CD34$^+$CD38$^-$ cells MACS enrichment kit, then 2 × 10^6 human CD34$^+$CD38$^-$ cells were injected into irradiated secondary recipients via the tail vein. 6 weeks later, secondary recipient mice were sacrificed and the engraftment of human bone marrow cells was analyzed by anti-human CD45, anti-human CD34 and anti-human CD38 staining.

METHOD DETAILS

Reagents and antibodies
Fluo4-AM, Rhod 2-AM, Alexa Fluor-488 goat anti-mouse IgG, Alexa Fluor-543 goat anti-rabbit IgG, Alexa Fluor-647 donkey anti-goat IgG and TRIzol reagent were purchased from Invitrogen (Carlsbad, CA). Rabbit anti-ORP4L, 3-MA and PIP$_2$ were from Sigma-Aldrich (St. Louis, MO). SDF-1α was from R&D Systems (Minneapolis, MN). Compounds C was from Merck Millipore (Billerica, MA). Kaempferol was purchased from Selleckchem. Alexa Fluor 647-anti-Ki67, Alexa Fluor 647-anti-human CD45, PE-anti-human CD34 and FITC-anti-human CD38 were obtained from BioLegend (San Diego, CA). Anti-pan-cadherin was from Santa Cruz (Santa Cruz, CA). Anti-PIP$_2$ and BODIPY® FL-PIP$_2$ were from echelon-inc. Anti-p-PDH was obtained from Novus (St. Louis, MO); anti-LC3, anti-p-AMPK, anti-PDH and anti-AMPK from Cell Signaling (Beverly, MA), and anti-actin from Proteintech Group (Chicago, IL).

Gene transfer
High-titer lentiviral stocks (above 10^9 TU/mL) carrying GFP-tag and shRNA-ORP4L, or ORP4L-cDNA were prepared by Shanghai GenePharma Co (Shanghai, China). The shRNA sequence can be found in Table S3. For lentivirus infection, 1 × 10^6 cells were resuspended in 100 μL medium containing lentivirus (Multiplicity of infection, MOI = 100) and 5 μg/mL polybrene in 24-well culture plates. Infections were carried out for 6 h at 37°C, 5% CO$_2$. After the end of infection, 400 μL medium was added. Knockdown or overexpression was verified by western blotting after 4 and 2 days' infection, respectively. For other gene transfers, cells were electroporated using Nucleofector^{TM} Kits for Human CD34$^+$ cells and 4D-Nucleofector^{TM} System (Lonza, Basel, Switzerland) according to the manufacturer's instructions. Functionality of cDNA overexpression by plasmid transfection was similarly verified by western blotting. Primer sequences used for cDNA subcloning into vectors are provided in Table S3.

Quantitative real-time PCR
Total RNA was isolated with TRIzol reagent (Invitrogen) according to the manufacturer's instructions. RNA samples were reverse transcribed using random hexamer primers in the presence of RNase inhibitor (Takara Bio, Shiga, Japan). qRT-PCR was performed with SYBR Premex EX Taq (Takara Bio) using the 7300 Sequence Detection System (Applied Biosystems, Foster City, CA). The data was filtered as follows: if the cycle threshold (C$_t$) score for sample was "Undetermined," or if the C$_t$ score was > 35, the score was set to 40 (McCall et al., 2014). A relative quantification analysis was performed using the ΔΔCt method, with actin as endogenous reference. Relative gene expression is presented as log (2$^{-\Delta\Delta Ct}$). Primer sequences used are provided in Table S3.

PM preparations
PM was prepared by using Plasma Membrane Protein Isolation and Cell Fractionation Kit (Invent Biotechnologies, Inc.) according to the manufacturer's instructions.

Lipidomics profiling by UPLC-HRMS
Freeze-dried cellular membrane samples were spiked with lipid internal standard solution (in methanol) containing lyso-phosphatidylcholine (LPC) 19:0, phosphatidylcholine (PC) (19:0/19:0), phosphatidylethanolamine (PE) (17:0/17:0), sphingomyelin (SM) (d18:1/12:0), triacylglycerol (TAG) (15:0/15:0/15:0), ceramide (Cer) (d18:1/17:0), free fatty acid (FFA) 16:0-d3 and FFA 18:0-d3. The mixture was vortexed for 1 min followed by addition of 1 mL of methyl tert-butyl ether and 15 min shaking. Then 250 μL of water was added for biphasic formation. The up-layer organic phase was collected and freeze-dried. The lipid residue was dissolved prior to analysis.

Cellular PM lipidomics profiling was performed in a Waters UPLC system coupled with a Q Exactive HF mass spectrometry (Thermo Fisher Scientific, Rockford, IL, U.S.A.) Chromatographic separation of lipids was achieved in a BEH C8 column (2.1 mm × 100 mm, 1.7 μm, Waters, Milford, MA, U.S.A.). The elution solvents consisted of A (ACN: H2O = 60:40, v/v) and B (IPA: ACN = 90:10, v/v), both contained 10 mM ammonium acetate. The elution composition started at 32% B for the initial 1.5 min followed by a linear increase to 85% B during the next 14 min, and then rapidly increased to 97% B at 15.6 min. After

2.4 min column flushing, the gradient was back to 32% B at 18.1 min, held for 1.9 min for column equilibration. The flow rate was 0.26 mL/min. The column temperature was set at 55°C. The sample manager temperature was set at 12°C.

Lipidomics data were acquired in both ESI positive and negative modes at scan ranges of 400 –1300 Da and 200 – 1800 Da, respectively. The spray voltage was 3.5 kV for positive mode and 3.0 kV for negative mode. The capillary temperature maintained at 300°C. The Auxiliary gas heater temperature was at 350°C. The flow rate of sheath gas and auxiliary gas was 45 arb and 10 arb, respectively. The S-lens RF level was 50. The AGC target and maximum IT were $3x10^6$ ions capacity and 100 ms for full MS scan, while were $1x10^5$ ions capacity and 50 ms for MS/MS scan. Mass resolution was set to be 120,000 and 30,000 for full scan MS and MS/MS. The TopN (N, the number of top most abundant ions for fragmentation) was set to 10. The normalized collision energy (NCE) was set to be a combination of 25, 35 and 45 eV.

Lipid identities were assigned based on accurate masses, retention time and/or MS/MS fragments. All detected lipids were quantified by normalization to the corresponding lipid internal standard. The lipid nomenclature follows the LIPID MAPS classification and nomenclature system.

Protein expression and purification

Open reading frames of cDNA were cloned into pGEX-4T-1 plasmid (Addgene, Cambridge, MA) and transformed into *E. coli* Rosetta™ (DE3) (Novagen), cultured at 37°C to OD_{600} 0.6-0.8, followed by induction with 0.5 mM IPTG for 16-18 h at 18°C. The Rosetta cells were collected and lyzed in cell lysis buffer (150 mM NaCl, 1% Triton X-100, 50 mM Tris-HCl, pH 8.0), containing with 1 mM phenylmethylsulfonyl fluoride (PMSF). Next, the samples were sonicated in a mixture of ice water with the following settings: (4 s on, 6 s off, 60% input, 4min), and centrifuged (10,000 x g for 20 min at 4°C) to obtain the soluble protein extracts. Add Glutathione Sepharose 4B beads (GE Healthcare) into the protein extracts according to the manufacturer's protocols. Washed the beads with cell lysis buffer and 50 mM Tris-HCl (pH 8.0) for 3 times, respectively. Finally, eluted the fusion protein with Glutathione reduced elution buffer (20mM Glutathione reduced in 50 mM Tris-HCl pH 8.0) and dialyzed against PBS. The purified GST fusion proteins were finally concentrated by Amicon Ultra-4 Centrifugal Filter Devices (Merck Millipore) and stored at −80°C.

Measurement of the kinetics of PIP_2 clearance

Cells seeded onto coverslips were incubated with 1 μM BODIPY® FL-PIP_2 (echelon-inc.com) for 10 min at room temperature in ECB (130 mM NaCl, 5 mM KCl, 1.5 mM $CaCl_2$, 1 mM $MgCl_2$, 25 mM HEPES, pH 7.5, 1 mg/mL BSA, and 5 mM glucose). The BODIPY® FL-PIP_2 images of cells were excited with low-intensity 488-nm laser excitation and acquired at 2 s intervals alternately under time-lapse mode by confocal microscopy (Zeiss LSM 510 Meta). The baseline fluorescence was collected 20 s before the ligand stimulation (500 ng/mL SDF-1α). Image data were subsequently analyzed using ImageJ (National Institutes of Health) and were presented as a ratio of F/F0 in the final results, where F0 represents baseline fluorescence intensity in each cell.

PIP_2 extraction assay

Cells were incubated with 1 μM PIP_2 (Sigma-Aldrich) for 10 min at room temperature in ECB before used for PM preparation. The assay mixture consisted of 50 μL of assay buffer (50 mM HEPES, pH 7.0, 100mM KCl, 6 mM $MgCl_2$, 0.6 mM $CaCl_2$, 2 mM EGTA) (Lomasney et al., 1996), 5 μg of GST-tag proteins and 10 μg of PM. The assay mixture was incubated at 37°C for 30 min. After the reaction, centrifuged and collected the PM in pellet for analysis of remaining PIP_2 by dot-blot. The suspension was incubated with Glutathione Sepharose for 1h at room temperature to pull-down the proteins and their binding PIP_2, centrifuged and collected the pellet for analysis of remaining PIP_2 by dot-blot (Figure 5I).

Reconstituted cell-free system

Cells were incubated with 1 μM PIP_2 (Sigma-Aldrich) for 10 min at room temperature in ECB and used for PM preparation. The assay mixture consisted of 50 μL of assay buffer (50mM HEPES, pH 7.0, 100 mM KCl, 6mM $MgCl_2$, 0.6 mM $CaCl_2$, 2 mM EGTA), 5 μg of GST-tag proteins and 10 μg of PM. The assay mixture was incubated on ice for 10 min, the reaction was started by the addition of GTPγS (50 μM) and incubation at 37°C for 10 min. After the reaction, centrifuged and collected the PM in pellet for analysis of remaining PIP_2 and DAG. The suspension was used for IP_3 generation (Figure 6A).

Dot blots for PIP_2 levels

The PIP_2 of PMs was released by incubation of lysis buffer (50 mM Tris, pH 7.5, 300 mM NaCl, 5 mM EGTA, 20 mM DTT, 2% Triton X-100 and 50 mM NaF) at 37°C for 30 min. Dot blots were conducted as described (Li et al., 2014). Briefly, after centrifugation, 1 μL of suspension was spotted onto nitrocellulose membrane (Bio-Rad Laboratories, Hercules, CA), probed with PIP_2 antibody (1:500, Echelon Biosciences) or PM internal loading control pan-cadherin antibody (Santa Cruz), and detected using a HRP-conjugated secondary antibody and enhanced chemiluminescence. Experiments were repeated at least three times.

Microscale thermophoresis

The protein concentration was diluted to 20 μM using the labeling buffer (50 mM HEPES with 150 mM NaCl, pH 8.0). Fluorescence labeling of ORP4L was performed following with the protocol of NT647-NHS using lysine residues. 100 μL of 60 μM NT647-NHS dye

was mixed with ORP4L at a 1:1 ratio followed by incubation for 30 min at room temperature in the dark. Unbound dye was removed by gel filtration on Sephadex G25 (GE Healthcare). The purity was monitored by measuring the ratio of protein to dye (spectroscopically by measuring absorption at 280 nm for the protein and 650 nm for the dye) after the clean-up procedure.

The concentrations of compounds were remained at 1 mM in a binding buffer (50 mM Tris-HCl, pH 7.4, 150 mM NaCl, 0.05% Tween-20). After 30 min incubation, the samples were loaded into microscale thermophoresis (MST)-grade glass capillaries. The intensities of the LED and laser were set at 40%. The MST analyses were performed using a Monolith NT.115 and the fitting curve was obtained using NTA analysis 1.4.23 via Hill fitting, and the KD is the numeric equivalent of the concentration of LYZ-81 or PIP_2 when the response is half of the plateau response (Rmax).

IP_3 and DAG measurement

IP_3 was measured using the HitHunter IP_3 Fluorescence Polarization Assay Kits (DiscoverRx Tech, Fremont, CA, USA) according to the manufacturer's instructions. For the DAG measurement, the PMs were disrupted by ultrasonication, after centrifugation, the suspension was used for analysis by using (DAG/DG) ELISA Kit (J&L Biological, ShangHai, China) according to the manufacturer's instructions.

Surface plasmon resonance assay

SPR experiments were carried out using a ProteOn XPR36 SPR instrument (BioRad Hercules, CA). Immobilization of proteins was performed using amine coupling to a General Layer Medium (GLM) (medium density) biosensor chip (BioRad). Standard amine coupling was used to immobilize proteins (20 nM in 10 mM sodium acetate buffer, pH 4.5) to the EDAC/Sulfo-NHS activated surface of a GLH biosensor chip (BioRad) at a density of 200-600 resonance units (RU) according to the manufacturer's instructions. After the injection of proteins, the surface was blocked with 1 M ethanolamine. The final immobilization level for proteins was approximately 12,000 RU. Compound was prepared in phosphate buffered saline, pH 7.4, containing 0.005% Tween-20 and injected at 100 mL/min for 250 s at concentrations of 10-0.625 μM (1:2 dilutions). Following compound injection, the chip surface was regenerated with 40 s pulses of running buffer. The compound concentration data collected were reference-subtracted using Biacore Evaluation software. Titrations were reference-subtracted using ProtedOn ManagerTM 2.0. Each titration was globally analyzed using the 1:1 Langmuir binding model to obtain the kinetic rate constants (k_{on} and k_{off}). The equilibrium dissociation constant (KD) was calculated from the rate constants. Global kinetic rate constants (k_a and k_d) were derived for each reaction, and the equilibrium dissociation constant, KD, was calculated using the equation KD = k_d / k_a.

Molecular docking

A homology model of ORP4L was generated based on a crystal structure of Osh3 ORD from *Saccharomyces* cerevisiae (PDB entry code: 4IC4) using Molecular Operating Environment (http://www.chemcomp.com) software. The sequences of these two models at the binding pocket area are highly conserved. Hydrogen atoms were added to the protein using the MOE modeling suite before carrying out the docking studies. Minimizing contacts for hydrogen, the structures were subjected to an Amber99 energy minimization protocol. The structure of LYZ-81 was energy-minimized, the atomic partial charges were calculated with the MMFF94s force field, and all possible ionization states were generated at pH 7.0. LYZ-81 was docked into the homology model using MOE; the binding site was modeled based on previous information on the sterol binding site (Im et al., 2005). The default Triangle Matcher was used as the placement method followed by force field refinement, and London ΔG scoring was used for the docking. The top-ranked conformation of the compound was selected for the ligand-receptor binding mode analysis (Clark and Labute, 2007).

MD simulation

The coordinates of PIP_2 were obtained from the crystal structure of Osh3 ORD in complex with PI(4)P from *Saccharomyces* cerevisiae (PDB code: 4INQ). ORP4L/PIP_2 complex was generated by superposing ORP4L and 4INQ. GPU-based (Götz et al., 2012; Salomon-Ferrer et al., 2013) MD simulations were performed on the ORP4L/PIP_2 complex and apo-ORP4L using the PMEMD module from AMBER 12 (D.A. Case et al., 2012).

The partial atomic charges of IP_3 were calculated through the Gaussian 09 (Frisch et al., 2009) program by using the Hartree-Fock method with the 6-31G(d) basis set. The Antechamber program was then used for fitting the restricted electrostatic potential (RESP) and assigning the GAFF force field parameters (Mukherjee et al., 2011). For the protein receptor ORP4L, the AMBER ff12SB force field was used (Cornell et al., 1995; Hornak et al., 2006). The ligand-receptor complex was neutralized by adding sodium/chlorine counter ions, and solvated in an octahedral box of TIP3P (Wang et al., 2006) water molecules with solvent layers 10 Å between the box edges and solute surface. The SHAKE (Miyamoto and Kollman, 1992; Ryckaert et al., 1977) algorithm was used to restrict all covalent bonds involving hydrogen atoms with a time step of 2 femtoseconds (fs). The Particle mesh Ewald (PME) method (Darden et al., 1993) was performed to treat long-range electrostatic interactions.

Three steps of minimization were performed before the heating step. All atoms were restrained with 50 kcal/(mol·Å2), whereas the solvent molecules were not restrained. This step included 2,000 cycles of steepest descent minimization and 2,000 cycles of conjugated gradient minimization. Second, all heavy atoms were restrained with 10 kcal/(mol·Å2) during the minimization steps, which

included 2,500 cycles of steepest descent minimization and 2,500 cycles of conjugated gradient minimization. The third step included 5,000 cycles of steepest descent minimization and 5,000 cycles of conjugated gradient minimization without restraint.

After the energy minimizations, the whole system was heated from 0 to 300 K in 50 picoseconds (ps) using Langevin dynamics at a constant volume and then equilibrated for 400 ps at a constant pressure of 1 atm. A weak constraint of 10 kcal/ (mol·Å2) was used to restrain all heavy atoms in the receptor-ligand complexes during the heating steps. Finally, periodic boundary dynamic simulations were conducted on the whole system with an NPT (constant composition, pressure, and temperature) ensemble at a constant pressure of 1 atm and 300 K in the production step. Each system was simulated for 100 ns. The coordinates of each system were saved every 4 ps. The root-mean-square deviations (RMSDs) of ORP4L, pocket loop (residues 520-540), and IP_3 were calculated. Clustering was applied to detect populated conformations with pairwise RMSD of 1.5 Å (Cα only) as the cutoff.

Binding energy calculation

The binding energies ($\Delta G_{binding}$) of IP_3 to ORP4L were calculated using MM/PBSA method from AmberTools suite in Equation (1):

$$\Delta G_{binding} = G_{epx} - \left(G_{rec} + G_{lig} \right) \tag{1}$$

where Gepx is receptor-ligand complex energy, Gepx is unbound receptor energy, and Glig is ligand energy.

MM-PBSA (Molecular Mechanics-Possion-Boltzmann/Surface Area) calculates the binding free energy considering the desolvation of the ligand and the unbound protein on the basis of a thermodynamic cycle. Equation (1) is also approximately calculated the follows:

$$\Delta G_{binding} = \Delta E_{MM} - T\Delta S + \Delta G_{sol} \tag{2}$$

$$\Delta E_{MM} = \Delta E^{ele} + \Delta E^{vdw} \tag{3}$$

where ΔEMM is the molecular mechanical energy obtained from the electrostatic (ΔE^{ele}) and the van der Waals (ΔE^{vdw}) interactions within the system, is the solute entropic contribution at temperature T (kelvin) and the solvation free energy (ΔG_{sol}) represents the electrostatic and nonpolar free energy of solvation. ΔG_{sol} is calculated inEquation (4):

$$\Delta G_{sol} = \Delta G_{sol}^{ele} + \Delta G_{sol}^{nonpolar} \tag{4}$$

where Δ_{sol}^{eel} is the polar contribution to solvation, and $\Delta G_{sol}^{nonpoular}$ is the nonpolar solvation term. The former component was calculated using the PB calculation, whereas the latter term is determined using Equation (5):

$$\Delta G_{sol}^{nonpolar} = \gamma SASA + b \tag{5}$$

where ^{SASA} is the solvent-accessible surface area (Å2) and γ and b represent experimental solvation parameters.

Steered MD simulation

Three different snapshots of ORP4L/IP_3 were taken from the MD simulation trajectories after the system reached stable. They were subjected for 2 ns SMD simulations where the restraint is time-dependent as in:

$$V_{rest}(t) = k[x - x_0(t)]^2$$

Where (x) is the distance of the specified atoms. SMD simulations were performed under the NVT ensemble. The maximal pulling distance was set to 10 Å between IP_3 and the binding pocket of ORP4L (Asn 600). In order to avoid any distortions of the protein due to pulling, the backbone of ORP4L was restrained with a force constant of 50 kcal/(mol·Å²). SMD simulations were repeated 3 times with different staring ORP4L/IP_3 complexes. By integrating the force over distance, a generalized work can be computed.

Co-immunoprecipitation

$CD34^+CD38^-$ KG1-α cells were washed twice with ice-cold PBS and incubated on ice for 30 min with 1 mL lysis buffer (50 mM Tris-Cl, 150 mM NaCl, 0.5 mM $MgCl_2$, 10% glycerol, and 0.5% Triton X-100, pH 8.0) supplemented with Protease Inhibitor Cocktail (Roche Group). Cell lysates were centrifuged for 10 min at 12,000 x g. The supernatant was preabsorbed for 1 h at 4°C with 50 μL of Protein G agarose (Invitrogen). The recovered supernatant was incubated overnight with ORP4L (3 μg; Sigma-Aldrich Cat#HPA021514) antibody at 4°C. 50 μL Protein G agarose was added to the lysate-antibody mixture and incubated at 4°C on a roller for 2 h. Agarose beads were washed four times with lysis buffer and boiled in 30 μL of SDS-PAGE loading buffer. Samples were resolved on 10% SDS-polyacrylamide gels and subjected to western blot analysis.

Immunofluorescence microscopy

For immunofluorescence staining of cells, cells seeded onto coverslips were stimulated with or without 500 ng/mL SDF-1α for 3 min and fixed with 4% paraformaldehyde for 30 min at room temperature, followed by permeabilization with 0.1% Triton X-100 for 5 min,

and blocked with 10% FBS for 30 min at room temperature. Cells were then incubated with primary antibodies in 5% FBS at 4°C overnight. After washing 3 times (10 min each) with PBS, cells were incubated with fluorophore-conjugated secondary antibody at 37°C for 30 min. The specimens were analyzed using a Zeiss (Oberkochen, Germany) LSM 510 Meta laser scanning confocal microscope system. For immunofluorescence staining of tissue sections, the sections were blocked with 10% BSA/PBS after microwave antigen retrieval and incubated for 2 h at room temperature with PE conjugated anti-Human CD34 antibody (1:50; Miltenyi Biotec Cat# 130-081-002) diluted in 5% BSA. After washing 3 times (10 min each) with PBS, the sections were mounted in fluorescence mounting medium (Invitrogen), and analyzed by confocal microscopy (Zeiss LSM 510 Meta laser system).

Imaging of parallel $[Ca^{2+}]_c$ and $[Ca^{2+}]_m$ oscillations

Cells (5×10^5 cells) were incubated with 2 μM Rhod-2 AM (for $[Ca^{2+}]_m$ measurement) for 60 min at 37°C in ECB. Then the cells were washed and re-loaded with 1 μM Fluo-4 AM (for $[Ca^{2+}]_c$ measurement) for additional 30 min at 37°C, followed by an additional 20 min incubation at 37°C to permit dye de-esterification. Then, cells were plated onto glass-bottomed dishes and the ECB was replaced by IMDM with 10% FBS. The $[Ca^{2+}]_c$ and $[Ca^{2+}]_m$ images of cells were excited with low-intensity 488-nm laser excitation (for Fluo-4 AM) and 516-nm laser excitation (for Rhod-2 AM) and acquired at 2 s intervals alternately under time-lapse mode by confocal microscopy (Zeiss LSM 510 Meta). Image data were subsequently analyzed using ImageJ (National Institutes of Health) and were presented as a ratio of F/F0 in the final results, where F0 represents baseline fluorescence intensity in each cell.

Extracellular flux assays and ATP measurements

Oxygen consumption was assessed using Oxygen Consumption Rate Assay Kit (MitoXpress-Xtra-HS Method; Cayman Chemical, Ann Arbor, MI), a porphyrin-based phosphorescent oxygen-sensitive probe. Prior to assay, cells were transferred into fresh culture medium containing 1% FBS. 10 μL of probe was added and the cells equilibrated at 37°C. The assay was read using a Microplate Reader (Synergy 4 Hybrid, BioTek, Winooski, VT). The maximal rate of oxygen consumption is proportional to the change in probe fluorescence during the linear phase of the assay. Cellular ATP levels were determined by ATP Bioluminescence Assay Kit CLS II (Roche, Basel, Switzerland) according to the manufacturer's instructions.

Cell cycle analysis

For evaluation of cell cycle profile, cells were fixed by the BD Fixation/Permeabilization kit (554714, BD Biosciences, San Jose, CA) according to the manufacturer's instructions, stained with Alexa Fluor 647-anti-Ki67 (1:100; BioLegend Cat# 350526) for 45 min at 4°C and re-suspended overnight at 4°C in 0.5 mL of 5 μg/mL 7-AAD staining solution (Thermo Fisher Scientific). Cells were analyzed by using flow cytometer (FACSAriaTM, BD) and the data were analyzed with the FlowJo_V10 software.

Cell death assay

Cell death was analyzed with the LIVE/DEAD® Fixable Far Red Dead Cell Stain Kit (Thermo Fisher, Waltham, MA) according to the manufacturer's instructions. Briefly, cells were washed once with PBS, and then incubated with LIVE/DEAD Fixable Dead Cell Stain in PBS for 30 min at room temperature in the dark. After washing with PBS with 1% FBS, cells were resuspended in PBS with 1% FBS and run on the flow cytometer (FACSAriaTM, BD) and the data were analyzed by FlowJo_V10 software.

In vitro colony forming assay

Cells were plated at 1×10^3 cells/plate in Methocult GF H4534 as described (Guzman et al., 2005). Plates were incubated at 37°C in a humidified atmosphere at 5% CO_2 and colonies were scored after 14 days of culture. Representative images from independent biological samples were shown in the figures.

Hematoxylin and eosin staining

Tissues were fixed and embedded in OCT embedding medium and sliced by frozen slicer (Leica CM1850, Wetzlar, Germany). The sections were stained with hematoxylin and eosin by using a standard protocol. Then, the stained sections were washed in 70% ethanol and imaged with industrial digital camera TOUPCAMTM (Hangzhou, China).

Western blot analysis

Cells were suspended in lysis buffer (50 mM Tris–Cl, pH8.0, 150 mM NaCl, 0.5 mM $MgCl_2$, 10% glycerol, 1% Triton X-100, 0.1% SDS) with protease inhibitor cocktail (Roche Diagnostics) on ice for 10 min. Samples were centrifuged for 10 min at 12,000 × g. The supernatants were collected and protein concentrations were measured by the BioRad (Hercules, CA) Dc Assay. Protein extracts were run on a 10% or 12% SDS polyacrylamide gel before transfer to a polyvinylidene difluoride membrane. Membranes were blocked with 5% milk for 1 h and incubated with primary antibodies overnight, followed by incubation with the secondary antibodies for 1 h at room temperature. Primary antibodies used in this study were: anti-ORP4L (1:1000; Sigma-Aldrich Cat#HPA021514), anti-Pyruvate Dehydrogenase E1-alpha subunit [p-Ser293] (1:1000; Novus Cat# NB110-93479), anti-Pyruvate Dehydrogenase (1:1000; Cell Signaling Technology Cat#2784), anti-ACTB (1:3000; Proteintech Group, Cat# 60008-1-Ig), anti-AMPK-alpha, phospho

(Thr172) (1:1000; Cell Signaling Technology Cat#2535), anti-AMPK (1:1000; Cell Signaling Technology Cat# 2603), anti-LC3B (1:1000; Cell Signaling Technology Cat#2775). The detection was carried out by enhanced chemiluminescence (Thermo Fisher Scientific).

QUANTIFICATION AND STATISTICAL ANALYSIS

All data is presented as mean ± SD. The value of n is mentioned in the figure legends and always stands for separate biological replicates. All *in vitro* experiments were repeated at least twice, and *in vivo* experiments were repeated at least once. All comparisons between groups were made by unpaired two-tailed Student's t test. Differences with * $p < 0.05$, **$p < 0.01$, and ***$p < 0.001$ were considered statistically significant. n.s., not significant.